Dynamics of amylopectin granule accumulation during the course of the chronic *Toxoplasma* infection is linked to intra-cyst bradyzoite replication.

Aashutosh Tripathi[1#], Ryan W. Donkin[1], Joy S. Miracle[1†], Robert D. Murphy[1^],
Abhijit Patwardhan[2] and Anthony P. Sinai[1*]

[1]Department of Microbiology, Immunology and Molecular Genetics,
University of Kentucky College of Medicine, Lexington, KY 40536, USA
[2] F. Joseph Halcomb III, MD. Department of Biomedical Engineering,
University of Kentucky College of Engineering, Lexington KY 40506, USA

Current Address:
[#] Department of Biochemistry, Stanford University School of Medicine, Palo Alto, CA 94305
[†] Department of Forestry and Natural Resources, Martin-Gatton College of Agriculture, Food and Environment, University of Kentucky, Lexington, KY 40546
[^] Maryland Department of Health, Laboratories Administration, Baltimore, MD 21205

* Corresponding Author: sinai@uky.edu

Running title: Amylopectin dynamics in chronic *T. gondii* infection

Abstract

The contribution of amylopectin granules (AG), comprised of a branched chain storage homopolymer of glucose, to the maintenance and progression of the chronic *Toxoplasma gondii* infection has remained undefined. Here we describe the role of AG in the physiology of encysted bradyzoites by using a custom developed imaging-based application AmyloQuant that permitted quantification of relative levels of AG within *in vivo* derived tissue cysts during the initiation and maturation of the chronic infection. Our findings establish that AG are dynamic entities, exhibiting considerable heterogeneity among tissue cysts at all post infection time points examined. Quantification of relative AG levels within tissue cysts exposes a previously unrecognized temporal cycle defined by distinct phases of AG accumulation and utilization over the first 6 weeks of the chronic phase. This AG cycle is temporally coordinated with overall bradyzoite mitochondrial activity implicating amylopectin in the maintenance and progression of the chronic infection. In addition, the staging of AG accumulation and it rapid utilization within encysted bradyzoites was associated with a burst of coordinated replication. As such our findings suggest that AG levels within individual bradyzoites, and across bradyzoites within tissue cysts may represent a key component in the licensing of bradyzoite replication, intimately linking stored metabolic potential to the course of the chronic infection. This extends the impact of AG beyond the previously assigned role that focused exclusively on parasite transmission. These findings force a fundamental reassessment of the chronic *Toxoplasma* infection, highlighting the critical need to address the temporal evolution of this crucial stage in the parasite life cycle.

49 **Introduction**

50 The broad host range and persistence of the protozoan parasite *Toxoplasma gondii* contribute
51 to its success as a pathogen (1 , 2). The ability of *Toxoplasma gondii* to form tissue cysts in its
52 asexual cycle is central to its long term persistence (3, 4). Tissue cysts serve as a vehicle for
53 transmission due to carnivory, with the option of entering the sexual cycle when the carnivore is
54 a felid (4). Tissue cysts contain several dozen to hundreds of genetically clonal organisms
55 termed bradyzoites (5, 6). Long considered to be dormant, our work established that encysted
56 bradyzoites retain considerable metabolic potential including the ability to replicate by
57 endodyogeny (3, 5).

58 Among the morphological features associated with encysted bradyzoites is the presence of
59 electron lucent cytoplasmic inclusions (7) that have subsequently been identified as
60 amylopectin granules (AG) (8-10). These inclusions, which are restricted to transmission forms
61 of the parasite, the bradyzoite and sporozoite, were noted to have their evolutionary origins with
62 the secondary endosymbiotic associated with the acquisition of the apicoplast, a relict genome
63 containing plastid derived for the ancestor of red alga (9, 11). In fact, the evolution of glycogen
64 and starch metabolism in eukaryotes provides molecular clues to the basis of plastid
65 endosymbiosis, linking them as is the case in Apicomplexa (12). The absence of AG within
66 tachyzoites, as well as the erroneous view that bradyzoites were replication incompetent,
67 cemented the view that AG did not play any role during the chronic infection (8, 13). Rather, AG
68 serves as a ready source of energy and metabolic potential to promote transmission to a new
69 host and/or reactivation events within the original host both of which are associated with
70 conversion to tachyzoites (8, 13). Our finding that bradyzoites are able to replicate within tissue
71 cysts (5) prompted us to examine whether AG played any role in the progression of the chronic
72 infection impacting energy metabolism and replication potential.

73 Early morphological data established that the levels and distribution of AG within encysted
74 bradyzoites is not uniform (7, 14, 15). To capture and quantify the relative levels of AG within

75 encysted bradyzoites we developed AmyloQuant, an imaging-based application to establish the
76 levels and distribution of AG within tissue cysts following optimized labeling with Periodic Acid
77 Schiff (PAS) reagent (16). Quantification of relative AG levels using AmyloQuant exposed a
78 remarkable level of diversity in AG across tissue cysts at all time points tested. The data
79 generated reveal that AG is dynamic, with patterns defining previously unrecognized phases in
80 the progression of the chronic infection within the infected murine brain. Furthermore, our data
81 establish that as a polymer of glucose, patterns for AG accumulation and breakdown correlate
82 with levels of bradyzoite mitochondrial activity and the capacity for both sporadic and
83 coordinated intra-cyst replication. These data suggest that such events are not random, but
84 rather are responsive to a potentially preprogrammed temporal cycle associated with the
85 progression of the chronic infection. Together these findings greatly expand our understanding
86 of the contribution of AG, revealing their role in the progression and maintenance of the chronic
87 infection by serving as a potential energy and metabolic resource to license demanding
88 processes, such as replication. We further find that the presence of a potential temporal AG
89 cycle reveals patterns in what otherwise appear as heterogenous populations governing overall
90 energetic, metabolic and replicative potential of the bradyzoites within tissue cysts. As
91 amylopectin dynamics emerge to play an important role in the normal progression of the chronic
92 infection, perturbation of this pathway may present an opportunity for therapeutic intervention
93 (17).

94 **Results**

95 **Amylopectin levels vary within encysted bradyzoites in vivo.**

96 Amylopectin granules (AG) were first recognized as electron lucent cytoplasmic inclusions within
97 encysted bradyzoites *in vivo* (7). AG is comprised of a branched homopolymer of glucose arranged as
98 repeating α1,4 linked chains interconnected with α1,6 branch points (**Fig. 1A**) (10). AG is similar to
99 plant starch and as such the parasite encodes all the genes needed for AG/starch synthesis (9, 18). AG
100 synthesis is initiated with glucose 6-P being converted to glucose 1 phosphate by

101 phosphoglucomutases (PGM1/2) (19, 20) which is activated with a UDP or ADP forming the nucleotide
102 sugar (21) that is the substrate for the starch/ glycogen synthase (8, 22). As the linear polymer and
103 branched chains are synthesized, chain winding results in the expulsion of water, generating a layer of
104 insoluble starch as the granule grows (18) (**Fig. 1B**). Mobilization of glucose from AG necessitates the
105 unwinding of the glucan chain, allowing access to amylases (23). This is facilitated by a glucan water
106 dikinase (TgGWD), a unique enzyme that transfers the β-phosphate from ATP to the glucan chain (21,
107 24, 25). As amylase progressively releases glucose, their progress is inhibited by the presence of the
108 phosphorylated glucose, necessitating the activity of a glucan phosphatase TgLaforin (17, 26, 27),
109 establishing a glucan phosphorylation- dephosphorylation cycle which, in conjunction with the
110 amylases, releases stored glucose for downstream functions.

111 Histologically stored glucans like glycogen (water soluble) and amylopectin can be detected using
112 Periodic Schiff reagent (PAS), where deposits are evident as a pink stain. In observing PAS-stained
113 tissue cysts within infected mouse brains, we confirmed considerable staining variability in tissue cysts
114 from the same animal (**Fig 1C**). The variations in labeling within tissue cysts confirm that while all the
115 housed bradyzoites are genetically clonal, they follow independent trajectories with regard to AG
116 accumulation. As a histological stain viewed with conventional light transmission microscopy, PAS
117 staining indicates the presence or absence of labeling but lacks, the sensitivity to measure relative
118 levels of AG based on staining. Chemically, the Schiff reagent is rosaniline hydrochloride, which early
119 spectroscopic studies established as brilliantly fluorescent across a broad range of the red spectrum
120 (16). We exploited this property to establish conditions for labeling purified tissue cysts, affording us an
121 optimal signal-to-noise ratio and linearity to capture differences in AG based on PAS staining (see
122 materials and methods).

123 **Relationship between AG levels and tissue cyst size.**

124 Tissue cysts *in vivo* exhibit a broad range of sizes regardless of their time of harvest (5). Historically,
125 tissue cyst size has been used as a measure to assess the effect of mutations, including those
126 associated with AG (21, 22, 28, 29) and pharmacological interventions (30-33). The relationship of AG

127 levels to cyst size was established by measuring the relative intensity following PAS staining of tissue
128 cysts purified at multiple time points (weekly between week 3 and 8 post infection). In pooling multiple
129 timepoints we sought to normalize the effect of the duration of the infection in our assessment. Purified
130 tissue cysts, labeled with FITC conjugated Dolichos lectin (DBA) and PAS were imaged at random with
131 30 cysts captured at each of the 6 weekly time points post infection. The images were acquired as
132 detailed in the materials and methods with the central slice of a z-stack (0.24μm thickness per slice) in
133 each channel used to determine the mean pixel intensity of the PAS signal and diameter based on DBA
134 demarcating the margins of the cyst using NIH Image J. Notably, the raw PAS signal without
135 deconvolution was used to determine the mean intensity because deconvolution resulted in the uneven
136 treatment of weak and strong signals to minimize background while accentuating positive signals (data
137 not shown).

138 As expected, tissue cyst dimensions varied dramatically within the acquired population with sizes
139 ranging from 15-85 μm in diameter (**Fig 2**). Given the overall distribution of sizes we categorized the
140 tissue cysts as small (<30μm), medium (30-60 μm) and large (>60μm) groupings (**Fig. 2**). Notably PAS
141 labeling in each group showed a similar distribution suggesting that tissue cyst size is not an effective
142 predictor of amylopectin levels (**Fig. 2AB**). We therefore examined whether the variability in AG
143 intensity across cysts was driven by the duration of the chronic infection. To address this we developed
144 AmyloQuant, an imaging based application to both quantify and map the relative distribution of AG
145 within tissue cysts based on the intensity of PAS staining.

146 **Development and implementation of AmyloQuant.**

147 The imaging based application AmyloQuant was developed to establish the intensity of PAS staining
148 and map its distribution within purified tissue cysts. Initial examination of histograms representing the
149 distribution of PAS intensity (AG concentration) revealed that the pattern could be efficiently defined by
150 4 intensity peaks representing: 1. Background (no labeling), 2. Low intensity pixels, 3. Intermediate
151 intensity pixels and 4. High intensity pixels. The setting of the initial thresholds defining each bin was

152 established using a modified Otsu threshold algorithm (34) to define the specific ranges. The final
153 output from this processing defines the fraction of pixels (relative to total pixels in the imaged volume)
154 belonging to each group. A detailed description of the development of AmyloQuant is presented in the
155 materials and methods.

156 A graphical user interface (GUI) was developed to facilitate the processing of PAS labeled cyst
157 images (**Fig. 3A**). An outline of the execution of the workflow to capture the levels of AG and their
158 distribution within purified ex vivo cysts is shown in **Fig 3B**. Following the acquisition of images using
159 identical exposure conditions within the experiment (detailed in materials and methods), the
160 AmyloQuant application identifies the location of the cyst within the image defining the region of interest
161 (ROI), which can be manually made larger or smaller using a slider allowing the user to make
162 adjustments to the automatically defined ROI. This isolates the imaged tissue cyst from the
163 surrounding pixels within the captured image, restricting the analysis to the defined ROI. Specific
164 threshold values defining the background, low and moderate thresholds define 4 bin's allowing for the
165 enumeration of pixels within each bin, from which the total pixel count and proportional pixel count in
166 each class can be determined (**Fig. 3AB**). The effect of altering these thresholds on individual tissue
167 cysts is presented in Supplementary Figure S1, highlighting the importance of standardizing the
168 thresholds to allow for comparative studies.

169 Additional standardization was needed by modifying the standard PAS staining protocol, which was
170 developed for largely histological but not fluorescence applications. Our analysis revealed that diluting
171 the Schiff reagent 1:10 provided optimal staining, affording the best dynamic range (**Fig 3C**). Tissue
172 cysts stained under optimal conditions were imaged using different exposure settings. In the example
173 presented we confirm the importance of standardization of exposure conditions as imaging the same
174 cyst with different exposure conditions results in vastly different spatial profiles **(Fig 3D**). Finally, given
175 that PAS can stain glucans other than AG, we employed GAA (Acid-Alpha Glucosidase) treatment to
176 selectively degrade AG and other glucose-based polymers (like glycogen) (**Fig. 3E**). Efficient

177 degradation of AG was noted by the observed loss of PAS labeling that was captured using
178 AmyloQuant (**Fig 3F**).

179 **The early course of the chronic infection is defined by a slow accumulation of AG.**

180 Tissue cysts within the infected animal are highly heterogeneous with regard to the tissue cyst burden,
181 size (5, 35), and replicative state (5). These characteristics vary further the longer the the chronic
182 infection persists, which is contrary to the long-prevailing notion that tissue cysts are dormant entities.
183 PAS staining of histological sections from chronically infected brains exhibits qualitative differences
184 (**Fig. 1C**), confirmed by a broad range of mean PAS intensity in purified cysts (**Fig. 2**), suggesting AG
185 levels are dynamic and likely to vary over the course of the infection. Quantification of either absolute
186 or relative AG levels within tissue cysts has not been undertaken. In addition, studies related to AG in
187 the chronic infection have focused on a single time point (typically 4 weeks post infection), with
188 observations inferred to apply the chronic infection in its entirely. To address these issues directly, we
189 leveraged our ability to quantify relative AG levels within tissue cysts using AmyloQuant, tracking them
190 weekly from week 3 to week 8 post-infection, defining the early chronic phase to a more established
191 state.

192 Tissue cysts purified from infected mouse brains at the indicated time points post infection were
193 deposited on slides, fixed with paraformaldehyde (36), and processed for PAS staining using the
194 optimized protocol. Images were acquired as z-stacks (0.24 microns), with the central stack selected for
195 quantification. Importantly, PAS quantification was performed on the raw image without deconvolution
196 as the application of image deconvolution algorithms (iterative and nearest neighbor) introduced visible
197 artifacts by artificially exaggerating differences in pixel intensity. Cyst images were acquired randomly
198 as they appeared on the slide and processed using AmyloQuant. Analysis, quantifying the number and
199 proportion of pixels in the background range (black- 0-10), low (blue- 10-25), intermediate (green- 25-
200 50), and high ranges (red >50) for each tissue cyst were plotted as a stacked plot (**Fig. 4**). Data from
201 30 randomly acquired tissue cysts were arrayed in an ordered progression from lowest intensity to
202 highest based on the levels of high-intensity (red) pixels. In order to increase the sensitivity in the high-

203 intensity range, a new set of bins was established in AmyloQuant with the ‘background” level set at a
204 grayscale threshold value of <50 (gray) and the high (red >50) range broken down into grayscale
205 values of 50-75 (light pink), 75-100 (dark pink) and >100 (100-254- purple).

206 While tissue cysts can be detected in the brain as early as 2 weeks post-infection, they tend to be
207 underdeveloped, lacking well-defined cyst walls (5). By 3 weeks post-infection, however, tissue cysts
208 can be readily recovered, making this time point widely viewed as the *de facto* onset of the chronic
209 infection (5). Consistent with being populated with bradyzoites, week 3 tissue cysts contain detectable
210 AG with variation in the relative level within tissue cysts accounting for the observed heterogeneity in
211 the population (**Fig. 4A**). In line with recent stage conversion, accumulation of AG within encysted
212 bradyzoites is limited as over two-thirds of the 30 arrayed cysts display low to low-intermediate intensity
213 values for PAS stained pixels (**Fig. 4A**)**.** While relatively uniform with regard to AG levels, 1 cyst out of
214 the 30 displays roughly 50% high-intensity pixels, with others display exceedingly small populations of
215 high-intensity pixels (**Fig. 4A**). Of note, all the high-intensity pixels are within the narrow 50-75
216 grayscale intensity value range (**Fig. 4B**). To get a sense of AG levels across the population of
217 analyzed week 3 cysts, we combined the values from all 30 cysts and classified them based on the pre-
218 set intensity intervals (**Fig. 4C**). The pie chart for the population confirms the proportions of pixels in
219 each class (**Fig. 4C**) and highlights that most of the high intensity pixels are all in a single tissue cyst
220 with all these pixels confined to the lowest positive interval within the high pixel range (**Fig. 4B**).
221 AmyloQuant generated heat maps showing the distribution of AG based on intensity class within the
222 arrayed sample confirms that intermediate intensity pixels are rare in the 10th cyst and increase in
223 proportion at cyst 15th further increasing to the point where there is a substantial proportion high-
224 intensity pixel (cyst 30/30) (**Fig. 4D**).

225 As the chronic infection progresses to week 4, we observe a marked shift in the proportion of the
226 intermediate PAS intensity population (green) coming at the expense of low-intensity (blue) pixels. As
227 such, this is consistent with a slow increase in AG accumulation that is likely dictated by the balance
228 between AG synthesis and turnover (**Fig 4E-H**). This population-wide shift is evident, with the

229 intermediate-intensity pixels representing 54% of the population. It is achieved by reducing the
230 proportion of low-intensity pixels relative to week 3. Thus, while there are fewer high-intensity pixels
231 (red), the increase in intermediate-intensity pixels is consistent with either the stabilization of AG levels
232 or, at most, a small increase. Thus, comparing week 3 and week 4, the time points at which most
233 studies on chronic infection are conducted, one might conclude that AG levels within encysted
234 bradyzoites have established an equilibrium.

235 Interrogation of week 5 derived tissue cysts challenges this assumption as we observe a marked
236 increase in both the number of intermediate level (green) pixels as well as the high intensity (red)
237 pixels. Indeed, 7 of 30 cysts have a significant accumulation of high-intensity pixels such that 9% of the
238 total pixels represent the high-intensity population (**Fig 4I-L**). Overall, the pattern is consistent with a
239 slow but steady increase in AG levels, representing stored metabolic potential potentially reserved for
240 downstream events.

241 **An unexpected burst in AG accumulation suggests a fundamental metabolic shift.**

242 Although our earlier work revealed an increase in the proportion of recently replicated bradyzoites
243 between weeks 5 and 8 (5), a potential role for AG and its stored glucose has not been explored. We,
244 therefore, applied the same methodology to examine tissue cysts harvested at week 6 post-infection
245 (**Fig 5A-D**). Within this population, we observed a marked increase in the proportion of tissue cysts
246 with significant levels of high-intensity pixels (cyst 14/30). This population included tissue cysts that
247 housed >70% of high-intensity pixels, including pixels in the 75-100 and even >100 intensity ranges.
248 On the opposite side of this spectrum, cyst 5/30 presented with only low-intensity pixels, a number that
249 appeared to reverse the trend for accumulation of AG, pointing to the dynamics not being unidirectional.
250 This raises the question of whether processes other than cyst expansion, such as reactivation events,
251 re-seeding events, and resetting the AG level, may occur at this time. Examining the distribution of PAS
252 intensities based on pixel number, a clear shift in the overall population is evident, with both low-
253 intensity and high-intensity populations increasing at the expense of the intermediate population relative
254 to week 5 (**Fig. 4C**). This points to AG dynamics not being unidirectional but rather driven by potentially

255 competing processes. As these studies capture the steady state at each time point for the population,
256 they may reflect distinct physiological demands imposing on AG synthesis and turnover, impacting net
257 accumulation.

258 The pattern at week 7 exhibits a profound increase in the accumulation of AG across all cysts
259 examined. Within the pool examined, cyst 21/30 had at least 10 percent of recorded pixels in the high-
260 intensity range (**Fig. 5E-H**). Among these, 5/30 had greater than 90% of pixels in the high-intensity
261 range, which included the majority of pixels in the >100 range. Viewed as a total population, over 58%
262 of pixels were in the high-intensity range, a marked increase from the 23% observed a week prior (**Fig.**
263 **5G**). The dramatic accumulation of AG in such a short time window compared to the kinetics across
264 other time points suggests specific priming of a potentially energy-intensive event.

265 **Rapid utilization of AG and the potential revelation of a programmed cycle**.

266 The accumulation of AG in weeks 6 and 7 failed to be sustained. Rather, tissue cysts harvested at
267 week 8 post-infection were marked by a plummeting of overall accumulated AG such that the patterns
268 and distribution across tissue cysts at this time mirrored cysts harvested at week 4 **(Fig. 4E-H**). Taken
269 together, the data suggest the presence of an underlying cycle related to AG that is likely connected to
270 other physiological events, including expansion of tissue cysts, potential disruption and re-seeding of
271 tissue cysts, and elevated levels of potentially synchronized intra-cyst replicative activity.

272 The data presented in Figures 4 and 5 are from a representative cohort of tissue cysts. In additional
273 studies including tissue cysts fixed with methanol (**Supplemental Data 2**) and cysts co-stained with
274 TgIMC3 antibody (**Supplemental Data 3**), with 30 cysts labeled at each time point the temporal pattern
275 for TgIMC3 is maintained. While the overall pattern is maintained, we found that fixation followed by
276 storage in methanol (-20°C) replicated the overall pattern with an overall muting of the PAS signal
277 (**Supplemental Data 2**). Thus, the temporal pattern for PAS labeling presented in the representative
278 experiments (**Fig. 4,5**) is confirmed with the staining of 90 cysts per time point.

279 **Correlation of AG dynamics to mitochondrial activity within tissue cysts**

280 As a storage homopolymer of glucose, amylopectin can be viewed as a reserve for energy and
281 biosynthetic needs. The single parasite mitochondrion {Seeber, 1998 #939}, like all typical
282 mitochondria, is engaged intimately integrated in intermediary metabolism. Fixable mitochondrion
283 targeting reagents like MitoTracker red allow for the selective labeling of active mitochondria within
284 diverse cells, including *Toxoplasma* (37). We established a protocol for the ex-vivo labeling of active
285 mitochondria within freshly isolated tissue cysts (materials and methods). Tissue cysts labeled with
286 MitoTracker display variable levels of labeling (38, 39) that can range from the absence of labeling to
287 very extensive labeling (**Fig. 6A)**. Most cysts, however, display a patchwork of labeled mitochondria
288 that do not reveal any specific pattern (**Fig. 6A)**. This diversity is notable as it indicates considerable
289 heterogeneity in levels of active mitochondria within tissue cysts and across cysts in the animal. We
290 developed MitoMorph, an imaging-based application to capture and classify mitochondrial forms based
291 on their morphology to capture this diversity (38, 39). In light of not all mitochondria within encysted
292 bradyzoites being active, the application captures and quantified nuclei within the imaged volume,
293 allowing for the number of active (MitoTracker positive) objects relative to the bradyzoite number
294 (number of nuclei) to be established (38, 39).

295 Periodic Acid Schiff reagent has an extremely broad fluorescence emission spectrum (16) that overlaps
296 the emission spectrum for MitoTracker Red (40) and significantly encroaches on the spectrum for
297 MitoTracker Orange (40). Notably, MitoTracker Green and other green emitting potential sensitive dyes
298 that do not spectrally overlap with PAS are not fixable (40), precluding any co-staining. PAS staining
299 was additionally found to interfere with DNA staining dyes like DAPI and Hoechst in a manner that
300 correlated with the overall PAS staining in the sample (**Supp Fig. S4**). The effects were variable,
301 resulting in the patchy loss of signal and significant artifactual labeling, as most commonly diffuse
302 staining that made imaging (using BradyCount) (5) as well as manual counting (using labeled counting
303 in Image J) inaccurate and subjective (data not shown). We, therefore, resorted to establishing the
304 levels of active mitochondria across the temporal progression of the chronic infection using matched
305 tissue cysts that were not stained with PAS.

306 Matched tissue cysts from the same harvests used for PAS staining were labeled with MitoTracker,
307 deposited on slides and fixed prior to staining with Hoescht dye (DNA). Tissue cysts were imaged
308 randomly using fixed image acquisition parameters as a z-stack in both channels. The stack was
309 subjected to deconvolution, and the center slice was used for analysis using MitoMorph (39). As
310 *Toxoplasma* contains a single mitochondrion (37, 41, 42), the ratio of 'active" (MitoTracker+) objects to
311 total nuclei within the imaged volume served as a surrogate for the proportion of active mitochondria
312 using the specific labeling conditions, acquisition parameters, and thresholds set in MitoMorph (39).

313 The early phase of the chronic infection (weeks 3-5), which is defined by the slow accumulation of AG
314 (**Fig. 4**), exhibited considerable diversity in the proportion of active mitochondria (**Fig. 6B**). While
315 statistically not different, the mean levels at week 5 are higher than those observed at weeks 3 and 4
316 (**Fig. 6B**). The proportion of active mitochondria within encysted bradyzoites at week 6 maintains the
317 levels observed at week 5 (**Fig. 6B**). Given the accumulation of AG between weeks 5 and 6 (**Fig. 4I-L**
318 **and Fig. 5A-D**), it suggests that AG-derived glucose, if involved in driving mitochondria activity, is
319 generated at a surplus level, driving storage despite utilization. The transition from weeks 6 to 7 is
320 noted by a dramatic statistically significant increase in the proportion of tissue cysts bearing highly
321 energized mitochondria (**Fig. 6B**). While 16% and 15% respectively of week 5 and 6 cysts have > 95%
322 of mitochondria active within the resident bradyzoite population, 47% of week 7 cysts have the same
323 active proportion (**Fig. 6B**). This burst of mitochondrial activity is accompanied by a similar burst in AG
324 accumulation (**Fig. 4,5**). In the absence of a way to directly correlate AG to the mitochondrial activity
325 within individual tissue cysts or bradyzoites due to the spectral overlap, direct correlations to explain
326 this convergence are impossible. However, supporting an integration of AG with overall mitochondrial
327 activity is the observation that the depletion of AG reserves between week 7 and 8 mirrors the effect
328 observed on the proportion of active mitochondria within week 8 cysts- which now mirror the distribution
329 at week 3, suggesting the resetting a cycle for mitochondrial activity.

330 **Establishing the relationship between AG dynamics and intracyst replicative status**

331 The intermediate complex protein TgIMC3 is highly expressed in developing daughter parasites during
332 endodyogeny (43, 44). Once a parasite is "born," the TgIMC3 signal is reduced to the point that it is no
333 longer detectable in the absence of the re-initiation of a replicative cycle (5). Thus, using quantitative
334 immunofluorescence, the intensity of TgIMC3 labeling can be used to establish the relative 'age" of
335 bradyzoite populations within tissue cysts. We previously used this metric by measuring the intensity
336 of tissue cysts early (Week 3), in the middle (Week 5), and at later time points (week 8) post-infection
337 (5).

338 In an ideal setting, measuring TgIMC3 intensity directly in PAS-stained samples would provide a direct
339 correlation between AG levels and the recency of replication. While we could capture TgIMC3 staining
340 in PAS-stained tissue cysts, we found the patterns erratic, especially at time points with high PAS
341 staining (**Supplemental Fig. 3 A,B**). We, therefore, undertook TgIMC3 staining of tissue cysts from
342 the same cohort of purified cysts at each time point in the absence of PAS staining and determined the
343 mean TgIMC3 intensity of individual tissue cysts using Image J (5) (**Fig. 6A, B**). These data
344 demonstrate significant differences in TgIMC3 intensity at weeks 4-7, with staining not being different at
345 weeks 3 and 8 when PAS labeling is at its lowest (**Supplemental Fig. 3B**). We, therefore, resorted to
346 addressing the time dependence of TgIMC3 in non-PAS-stained tissue cysts to correlate with prep and
347 time point-matched PAS-stained samples (**Fig. 2,4,5**).

348 Consistent with our prior findings (5), we observed a marked reduction in the overall TgIMC3 intensity
349 between weeks 3 and 5 (**Fig. 7A, B**). Images of representative high-intensity, mean-intensity, and low-
350 intensity cysts at each time point expose the diversity of the TgIMC3 signal (**Fig 7A**). Interestingly,
351 tissue cysts at week 4 reveal that the bulk of the reduction in the TgIMC3 signal happens between
352 weeks 3-4 and is sustained at week 5. This is entirely consistent with a progression toward a lower
353 replicative state. In our earlier work, we posited that the increase in TgIMC3 intensity between weeks 5
354 and 8 could be due to a gradual increase across this time frame or, alternatively, an episodic burst of
355 replicative activity and its subsequent stabilization (5). The data are consistent with the latter possibility

356 as we observe a marked increase in mean TgIMC3 intensity across imaged cysts sustained at week 7,
357 settling at an intermediate level between weeks 3 and 5 at week 8, thus matching our prior data (5).

358 **Depletion of AG between weeks 7 and 8 correlates with a burst of intra-cyst replication**.

359 The packing density, which reflects the occupancy of tissue cysts, provides a measure by which cysts
360 of different sizes can be compared with regard to their relative bradyzoite burden (5). This measure is
361 based on the enumeration of nuclei within the imaged volume (5). In this study, we used a fixed z-step
362 in image acquisition for all cysts regardless of size, allowing for the area encompassed by the margins
363 of the cyst to suffice in determining the packing density.

364 Due to the interference of PAS with nuclear staining (**Supplemental Fig. S4**), the reliability of
365 determining the packing density of PAS-stained tissue cysts is in question. We, therefore, used the
366 cohort of tissue cysts used for the TgIMC3 intensity (**Fig. 7A,B**) measurements to establish the packing
367 density (PD) distribution from weeks 3-8 (**Fig. 7C**). While the impact of recent replicative events
368 captured with TgIMC3 intensity will, in general, increase the packing density, how it is reflected in the
369 data will depend on the proportion of replicating bradyzoites as well as the actual recency of the event.
370 This effect can, therefore, be muted when measuring the overall mean intensity of TgIMC3 such that
371 low-level replication events may be difficult to resolve whole coordinated recent replication of a
372 substantial proportion of bradyzoites (**Fig. 7AB**).

373 The packing density distribution while variable showed no statistical difference between weeks 3 and 6
374 for all pairwise relationships (**Fig. 7C**). The packing density was however statistically significant
375 between week 3 and week 7 purified cysts, but not between the intervening weeks and week 7 (**Fig.
376 7C**). Cysts at week 7 have the lowest mean PD following a trend from week 3. This pattern is
377 completely reversed between week 7 and 8 resulting in a highly significant increase the PD, indicating a
378 large scale potentially coordinated replication event across tissue cysts within this time interval (**Fig.
379 7C**). Notable here is that this coordinated burst in intra-cyst replicative activity is temporally connected
380 to the dramatic loss of AG (**Fig. 5**) and overall mitochondrial activity (**Fig. 6**).

381 **Discussion**

382 Storage glucans like glycogen in animals and starch in plants are used as energy/ metabolic reserves
383 that are charged under conditions of low demand as a resource for future energy and metabolite
384 intensive processes (45-47). In *Toxoplasma* , cytoplasmic amylopectin granules (AG), are more similar
385 to insoluble plant starch than soluble animal glycogen (9). AG are associated with transmission stages,
386 including encysted bradyzoites and sporozoites (4, 8, 9), but not with rapidly replicating tachyzoites,
387 which appear to contain a more labile glycogen-like storage glucan (27). The association of AG with
388 transmission forms had led to the view that their primary, if not sole purpose, is to provide and energy/
389 metabolite resource to be deployed upon transmission and differentiation into replicative tachyzoites (6,
390 28). Our work (5), that challenged the long prevailing dogma of bradyzoites lacking replicative
391 potential, presented the possibility that AG could be used during the chronic infection as an energy/
392 metabolite resource to promote energy intensive processes, including intra-cyst bradyzoite replication.

393 Studies on the chronic infection (including those focused on the AG pathway) have, and continue to be
394 focused on the tissue cyst, with tissue cyst burden (6, 22, 28, 29, 48) and size (6, 22, 28-30, 48) serving
395 as measures of the extent of the chronic infection. Both measures can be highly variable even in the
396 absence of any genetic or pharmacological intervention making them less than ideal metrics (5, 35).
397 Indeed, following the analysis of a potential relationship between mean AG levels based on PAS
398 intensity and size, we are unable to define any significant correlation functionally linking the two (**Fig.
399 2**). This points to the need to quantify the distribution of AG within individual cysts, to more robustly and
400 accurately, address AG levels in the progression of the chronic infection.

401 With our introduction of imaging-based approaches we can effectively deconstruct tissue cysts to the
402 level of encysted bradyzoites, addressing bradyzoite occupancy (5) and mitochondrial
403 activity/morphology (38, 39). In this study we leveraged our experience with imaging-based
404 approaches to address the dynamics of AG during the course of the early and maturing chronic
405 infection following staining with an optimized PAS labeling protocol. We developed AmyloQuant, an
406 imaging-based application allowing for the capture of PAS fluorescence intensity to measure and map

407 relative AG levels within tissue cysts (**Fig. 3**). This application has exposed AG to be considerably
408 more dynamic than previously imagined. First, tissue cysts display considerable heterogeneity in both
409 the levels and distribution of AG at every time point and within every tissue cyst prep (**Fig. 4,5**, **Suppl**
410 **S2**). This diversity of AG levels within tissue cysts is made more remarkable given that every tissue cyst
411 is genetically clonal having originated from the infection of single parasite. This deviation from
412 uniformity is likely the outcome the loss of replicative synchrony noted in *in vitro* bradyzoites (49, 50)
413 leading to the establishment of distinct physiological trajectories within the same tissue cyst.

414 Most studies on the chronic infection examine a single time point typically between 3-5 weeks post
415 infection, with analysis restricted to the tissue cyst burden. These studies treat tissue cysts as uniform
416 entities despite clear evidence that they differ greatly in size and bradyzoite occupancy (5). In our
417 earlier work (5), we undertook analyses to determine the progression of the chronic infection which led
418 to the finding that the onset of the chronic infection at week 3 post infection was marked by evidence of
419 considerable replicative activity based on overall labeling with TgIMC3 (5), a marker for the recency of
420 replication {Anderson-White, 2011 #534}. The proportion of recently replicated bradyzoites within cysts
421 plummeted by week 5 but showed a partial resurgence at week 8 post infection (5). Building on the
422 skeleton of this potential cycle we determined the relative amylopectin levels within tissue cysts
423 harvested weekly between weeks 3 and 8 using AmyloQuant (**Fig. 3,4,5, Suppl S2**). Not surprisingly,
424 recently formed bradyzoites at the onset of the chronic phase (week 3) contained relatively low levels of
425 AG accumulation (**Fig. 4**). During this phase we observe a steady increase in accumulation of AG with
426 considerable diversity in AG levels between cysts at each time point (**Fig. 4**). This cyst to cyst variability
427 can be partially explained by the fact that stage conversion in the brain is affected by the kinetics of
428 parasite tropism to the brain as well the efficiency of conversion to the encysted state.

429 In our earlier work, we noted that tissue cysts harvested at week 8 possessed evidence of recent
430 replicative activity that was intermediate that seen at weeks 3 and 5 respectively (5). When we
431 measured the changes in AG levels at weeks 6 and 7 we were surprised by the rapid accumulation of
432 AG initiated at week 6 and progressed through week 7 (**Fig . 5**). Notably the increases in AG levels

433 were not uniform for all cysts, pointing to the physiological and metabolic heterogeneity of the encysted
434 bradyzoites (**Fig. 5**). Despite this heterogeneity however, the overall population of cysts and by
435 extension, the resident bradyzoite population, exposed a potentially pre-programmed response
436 whereby the steady accumulation of AG in weeks 3-5 (**Fig. 4**) is punctuated by a burst of AG storage at
437 weeks 6-7 (**Fig. 5**). Such potentially pre-programmed storage of AG is a likely harbinger for significant
438 energy/metabolic-intensive events. Rapid utilization of AG from high levels at week 7 to levels at week
439 8 observed early in the chronic infection (weeks 3-4) (**Fig. 4,5**), suggest the resetting of a potential AG-
440 cycle.

441 The conversion of tachyzoites to bradyzoites in cell culture is associated with a decrease in the
442 mitochondrial membrane potential (51). Imaging of ex vivo tissue cysts labeled with MitoTracker
443 revealed a considerable level of heterogeneity for both mitochondrial activity and morphology (39).
444 This heterogeneity in mitochondrial activity within tissue cysts is evident from the proportion of
445 bradyzoites that label with MitoTracker (**Fig. 6**). Since the parasite contains a single mitochondrion
446 {Seeber, 1998 #939}, this ratio can be quantified by counting the number of labeled mitochondrial
447 profiles relative to the number of nuclei within the imaged volume (**Fig. 6B**). As expected, the
448 proportion MitoTracker labeled mitochondrial profiles varied significantly from cyst to cyst (**Fig. 6AB**)
449 but showed a generally increasing pattern from week 3-6 (**Fig. 6B**). Coincident with the sharp increase
450 in AG, the transition from week 6 to 7 (**Fig. 5**) correlated with a significant increase in the proportion
451 number of tissue cysts with virtually all mitochondrial profiles active (**Fig. 6**). This suggests a tight
452 functional connection between AG accumulation and mitochondrial activity suggesting with AG
453 accumulation and turnover liberating glucose to drive the membrane potential ($\Delta\Psi m$). This relationship
454 is reinforced as the apparent utilization AG noted by the precipitous drop in its levels between weeks 7
455 and 8 (**Fig. 5**) is mirrored with a concomitant decrease in the proportion of active mitochondria within
456 the encysted bradyzoite population (**Fig. 6**).

457 Such dramatic shifts in both stored energy and energy utilization would only make logical sense if
458 applied to an energy intensive process such as replication. We therefore determined the level of

459 TgIMC3 labeling from week 3-8 (**Fig. 7**). We found that the harshness of PAS treatment had differential
460 effects on TgIMC3 labeling based on AG levels (**Supplemental Fig. S3**). Additional effects were
461 noted with regard to the quality of the DAPI labeling to establish nuclear counts (**Supplemental Fig.**
462 **S4**). We therefore examined TgIMC3 labeling from week 3-8 on an independent cohort of matched
463 tissue cysts. Consistent with earlier data (5) we observed high TgIMC3 levels at week 3 with a marked
464 decrease at weeks 4 and 5 indicating a marked reduction in recent replication (**Fig. 7B**). The rapid
465 accumulation of AG at weeks 6-7 coincided with an increase in active replication within tissue cysts that
466 was maintained at week 8, at a level between that for weeks 3 and 5 (**Fig. 7B**), thus replicating earlier
467 findings (5).

468 We next established the packing density of bradyzoites as a function of the progression of the chronic
469 infection in this cohort of tissue cysts. The packing density allows for the comparison of tissue cysts of
470 different sizes (5), with a higher packing density correlating with significant intra-cyst replication.
471 Although there is clear evidence for an increase in recent replication between weeks 5-7 (**Fig. 7AB**),
472 the increases appear to be distributed between tissue cysts in a manner that does not significantly alter
473 the packing density (**Fig. 7C**). This is in sharp contrast to the events between week 7 and 8 which is
474 marked by a more highly synchronized mass replication event resulting in a dramatic increase in the
475 packing density (**Fig. 7C**). This highly coordinated replicative burst of bradyzoites within tissue cysts
476 appears to be the culmination of a build-up of events within which AG plays an important role. Toward
477 comparing the temporal progression of the chronic infection based on the measured physiological
478 parameters, we plotted the mean (+/- SEM) for each parameter as a function of time (week post-
479 infection), separating the early (weeks 3-5) and later (weeks 6-8) time points (**Fig. 8**). Together, the
480 data paint a picture of the dynamics of AG and that the proportion of active mitochondria is very similar,
481 suggesting an integration of AG levels with overall mitochondrial activity (**Fig. 8**). The loss of recent
482 replicative activity between weeks 3-5 correlates with an overall lower level of AG and its slow
483 accumulation (**Fig. 8**). The overall increase in recent replicative activity in the second phase of the cycle
484 is mirrored by the rapid accumulation and subsequent depletion of AG (**Fig. 8**). This replicative phase,

485 while evident with the burst in the packing density at week 8 appears to involve the culmination of
486 events initiated at week 6 as part of a coordinated process (**Fig. 8**).

487 In light of the centrality of glucose in intermediary metabolism, a role for stored glucose in the form of
488 AG is not surprising. Its importance is highlighted with the analysis of several mutants involved in both
489 the synthesis and turnover of amylopectin. Interference at the level of AG synthesis, targeting genes
490 commitment step to starch synthesis the UDP-sugar pyrophosphorylase (TgUSP, TgUDP-GPP/
491 UGPase (TgME49_218200) (21) or Starch/glycogen Synthase (TgSS-TgME49_222800) all result in a
492 lower cyst recovery (22), and further hint toward a defect in reactivation based on cell culture based
493 studies (22). In contrast, deletion of the Starch branching enzyme (TgSBE1-TgME49_316520) failed to
494 have any impact on tissue cyst recovery (52). The cyst burden is dependent on the successful
495 navigation of the acute infection, tropism to the brain, stage conversion and subsequent development in
496 the chronic phase. Thus any phenotype assessed at the level of the cyst burden can manifest at one or
497 several of these steps. With the typical assessment of phenotypes at 28-30 days post infection (week
498 4), the true effect of the AG defect may not have yet fully manifested, leaving open the possibility of
499 more significant impacts than currently reported.

500 Steady state levels of AG are dictated by the effects of both synthesis and degradation. Deletion of
501 starch degrading α-amylase (Tg-αAMY- TgME49_246690) resulted in an overall reduction of the tissue
502 cyst burden (53). The dynamics of AG indicate a level of regulatory control for which the Calcium
503 Dependent Protein Kinase TgCDPK2 (TgME49_225490) has emerged as key component (48).
504 Deletion of this gene results in aberrant accumulation of AG in tachyzoites and within in vitro
505 bradyzoites (48). Loss of TgCDPK2 is reported to eliminate tissue cysts, although these data need to
506 be viewed with caution on account of the low reported cyst yields in animals infected with the wild type
507 Pru strain (48). The protein phosphatase PP2A-holoezyme, has been shown to dephosphorylate
508 TgCDPK2 affecting its activity (54, 55). Ablation of TgPP2A holoenzyme in the ME49 background
509 similarly resulted in the loss of tissue cysts (54, 55). Based on transcriptomic studies, and differential
510 phoshoproteomics, regulation appears to be occurring at the levels of both AG synthesis and turnover

511 (54, 55). This is not surprising for a storage molecule as the overall regulatory environment needs to be
512 programmed for either the “charging” or ‘discharge” of the battery.

513 Efficient AG degradation is dependent on reversible glucan phosphorylation catalyzed by the kinase-
514 phosphatase pair of the glucan water di-kinase TgGWD (TgME49_214260) (21) and the phosphatase
515 TgLaforin (TgLAF, TgME49_205290) (17, 27). Direct phosphorylation of the glucan chain by GWD
516 facilitates unwinding allowing amylase-mediated degradation to the point of phosphorylation (23, 24,
517 56) (**Fig. 1B**). TgLaforin, by removing the phosphate from the glucan chain allows for starch
518 degradation to proceed (17, 23). Loss of either TgGWD or TgLaforin is predicted to produce a starch
519 (or glycogen) excess phenotype based on findings from algae to higher plants and animals including
520 mammals (23, 56, 57). Consistent with a role for AG in the chronic infection deletion of TgGWD (21) or
521 TgLaforin (TgLAF) (27) results in a reduction in the overall cyst burden. The effect of the loss of
522 TgLaforin on AG accumulation was found to be nuanced revealing a temporal dimension (27). Notably,
523 the ∆TgLAF mutation did not have a significant impact on AG, based on PAS and AmyloQuant analysis
524 at week 4 post infection (27). In contrast, ∆TgLAF tissue cysts harvested at week 6, displayed a
525 marked increase in the levels of AG accumulation relative to WT or complemented tissue cysts (27).
526 This is notable as at week 6 both an increase in AG levels and recent replication (based on TgIMC3)
527 are evident (**Fig. 8**) pointing to an imbalance caused by the expected reduction in the efficiency of AG
528 turnover. This exaggerated accumulation of AG is reflected in electron microscopic analysis which
529 reveal bradyzoites filled with AG that are enucleated and/or appear dead (27). Furthermore, these data
530 indicate that the AG pathway is potentially druggable, with the effectiveness of potential small
531 molecules being linked to the specific physiological state of bradyzoites along its temporal cycle (17).
532 Not surprisingly, given the emerging importance of the physiological state of encysted bradyzoites is
533 that a clear correlation emerges with regard to the levels of AG and the proportion of ‘active”
534 mitochondria within tissue cysts (**Fig. 4, 5, 6**). Further functional connections of AG to both episodic and
535 synchronized replication events (TgIMC3 intensity) reflected in changes in the packing density point to
536 a central role for AG (**Fig. 7,8**).

537 A role for stored glucans in the regulation of replicative cycles is evident in the plant kingdom from
538 photosynthetic algae to higher plants (58-60). In general, starch accumulates during the light cycle, but
539 supports anabolic and replicative functions during the dark cycle (58-60). For example, in *Euglena*
540 *gracilis*, light exposure just before subjective 'dusk" is most effective in the commitment to cell division,
541 while exposure to light close to subjective 'dawn" is not (61). Licensing of this commitment is intimately
542 linked to levels of stored starch (61). While light exposure cannot be a factor in dictating the
543 commitment to replication, immuno-metabolic cues associate with the development and maintenance of
544 immune pressure within the host are likely to be sensed and responded to. The transition from
545 tachyzoite to bradyzoites has long been associated with the establishment of the adaptive immune
546 response (reviewed in (62, 63)). More recent work on the maintenance of immune pressure, mediated
547 predominantly by effector T populations and key cytokines like interferon gamma indicates that this
548 response is dynamic (reviewed in (64, 65)). Notable here, is the finding that as the chronic infection
549 progresses, both resident and peripheral T cells exhibit a loss of effector functions correlating with the
550 emergence of suppressive markers of T cell exhaustion (64-67). The emergence of these markers
551 evident from the direct examination of *Toxoplasma* directed T cell populations and transcriptomic
552 analyses (64, 65, 67). This decrease in specific immune pressure coincides with the apparent
553 reprogramming of the AG pathway noted by a rapid accumulation of AG between weeks 5-7
554 culminating in its apparent utilization between weeks 7-8 (**Fig. 5,8**). With temporal changes in relative
555 mitochondrial (**Fig. 6,8**) and replicative activity (**Fig. 7,8**), suggest an integrated response within
556 encysted bradyzoites.

557 While the specific triggering signal remains unclear, the apparent temporal changes in immune status
558 are the potential mediators governing AG accumulation and utilization, analogous to light in algae and
559 plants (58-60). As a potential cycle, it is tempting to speculate that spontaneous reactivation events,
560 while controlled, serve to re-invigorate the immune response, potentially tailoring it toward bradyzoite
561 directed antigens thereby establishing a new détente. This new détente could alter the progression
562 through the subsequent temporal cycle, shortening it, lengthening it or maintaining it unchanged. Such

563 an integrated interplay would explain the well established role of the mouse strain on the tissue cyst
564 burden as well as susceptibility to reactivation and associated symptomology during the progression of
565 the chronic infection (68-70). Additionally, it would explain the “life-long persistence” of *Toxoplasma* ,
566 with one critical caveat. The encysted bradyzoites that persist are unlikely to be the original parasites
567 establishing the infection but rather their descendants following cycles of reactivation and re-seeding.

568 In summation, with this study we expose the dynamics of AG accumulation over the first 6 weeks of the
569 chronic *Toxoplasma* infection. In examining this time course, we reveal a previously unrecognized
570 temporal progression that links AG to overall mitochondrial and replicative activities. Unlike tachyzoites
571 bradyzoites demonstrate and high degree of physiological and metabolic heterogeneity that dictates
572 their capacity to replicate (71). These data suggest that AG may serve as a critical metabolic licensing
573 factor, necessitating a minimal level to permit replication of encysted bradyzoites. Thus, while sporadic
574 replication occurs in individual bradyzoites, coordinated large scale replication events require robust
575 coordinated AG accumulation as observed in week 6-7 (**Fig. 5**). The finding that bradyzoites are
576 physiologically heterogenous within and across tissue cysts, yet demonstrate a clear temporal
577 progression exposed by AG dynamics suggests functional entrainment likely co-evolving with the
578 immuno-metabolomic status of the host. These findings further reinforce the view that the chronic
579 *Toxoplasma* infection, is an active rather than a dormant phase in the life cycle that simply operates on
580 a longer time scale. This fact needs to be integrated into the design of future studies related to the
581 chronic infection as investigations single time points provide a very limited view, that should not be
582 inferred as applying to the entire life cycle stage.

583 **Materials and Methods:**

584 **Generation and purification of tissue cysts:** CBA/J mice of both sexes (Jackson
585 Laboratories, Bar Harbor, ME) were injected intraperitoneally with 20 Type II ME49ΔHXGPRT
586 tissue cysts as previously described (35). Details regarding husbandry of infected animals
587 including monitoring for symptoms and euthanasia were conducted as previously described (5,
588 35, 36). Tissue cysts were purified at weeks 3,4,5,6,7, and 8 post infection. In each instance
589 purifications were done two days following the completion of the week (for example: Week 3:
590 day 23). All protocols were carried out under the approval of the University of Kentucky's
591 Institutional Animal Care and Use Committee (IACUC).

592 **Histology of infected mouse brains:** Brains from chronically infected mice were harvested
593 intact and fixed in Neutral Buffered Formalin (10% formalin in PBS) for 24 hours and stored in
594 70% Ethanol. Individual hemispheres were paraffin embedded and 5μm sections generated
595 and fixed on slides. Sections were sequentially stained with hematoxylin and PAS at the
596 Biospecimen Procurement and Translational Pathology Shared Resource Facility at the
597 University of Kentucky Markey Cancer Center using standard protocols. Stained sections were
598 imaged using a full spectrum Zeiss Axiocam 208 color camera on a Zeiss stand as described
599 below.

600 **Tissue cyst purification**: Tissue cysts were recovered from infected brains at the indicated
601 time points with 2 brains being processed for each prep as described in detail (36). Purified
602 tissue cysts were obtained from the infected brain homogenate using a discontinuous Percoll
603 gradient and quantified following fractionation of as previously described (36). Recovered
604 tissue cysts were pelleted onto glass slides (200-300 cysts/slide) and fixed in either 4%
605 paraformaldehyde in PBS for 30 minutes or in absolute methanol at -20°C as indicated.
606 Paraformaldehyde fixed tissue cysts on slides were stored in PBS at 4°C while methanol fixed
607 slides were stored in absolute methanol at -20°C prior to labeling.

608

609

610 **Periodic Acid-Schiff (PAS) labeling of tissue cysts:**

611 The tissue cysts purified from the infected mouse brain were centrifuged and deposited on a
612 glass slide using a Cytospin centrifuge (36). The cyst deposited on the glass slide was fixed
613 either in methanol (100%, stored at -20 ˚C) or in paraformaldehyde (PFA) (4% in phosphate-
614 buffered saline (PBS). Tissue cysts fixed in PFA were permeabilized in 0.1% triton solution in
615 PBS^{++}((PBS containing 0.5 mM $MgCl_2$) for 10 minutes. The tissue cysts fixed in methanol were
616 proceeded for PAS staining. The sample was washed thrice in tap water in a caplin jar and
617 incubated with 0.5% of periodic acid (Newcom Supply, cat# 13308A) for exactly 5 minutes. For
618 the optimized labeling protocol Schiff's reagent (Newcom Supply, Cat# 1371A) was diluted
619 1:10 in tap water and added to the slide in the dark for exactly 10 minutes. Other dilutions
620 tested were 1:4 (Manufacturers recommendation) and 1:20. The slides were transferred to a
621 Coplin jar and washed 10 times with tap water. Slides were subsequently counterstained with
622 DAPI to image nuclei. As noted in the results, the harsh conditions of Periodic-Schiff regent
623 caused interference with the labeling of some antibodies including a rat anti-TgIMC3 antibody
624 (Donkin et al. in preparation). In addition, high intensity PAS labeling resulted in the distortion
625 of the nuclear staining patterns. For these reasons, the labeling and quantification of these
626 signals was performed in tissue cysts from the same preps that were not PAS labeled. Notably
627 staining with *Dolichos biflorus* lectin was not impacted by PAS.

628

629 **MitoTracker labeling of *ex vivo* tissue cysts:** Pooled Percoll fractions containing greater
630 than 2500 tissue cysts were diluted 1:5 with Artificial Intracellular Salts Buffer (AISS) (72) and
631 the cysts pelleted for 5 minutes at 2000 rpm at ambient temperature in a sterile 15ml conical
632 tube. The supernatant was aspirated leaving roughly 250μl into which the tissue cyst pellet
633 (that may not be clearly visible) was resuspended. 2.75ml of Prewarmed AISS buffer with 25nM
634 MitoTracker was added and the tube incubated within a pre-warmed water bath in the incubator
635 for 45 minutes. The tube was mixed every 15 minutes. Following this incubation 12ml of
636 prewarmed AISS was added to chase the MitoTracker and incubated for an additional 30

637 minutes. The labeled tissue cyst were deposited on glass slides using a Cytospin centrifuge
638 as previously described and fixed in 4%PFA (36), prior to storage as described above. Cyst
639 nuclei were labeled using DAPI prior to imaging as described below.
640
641 **Immunofluorescence labeling**: PFA fixed tissue cysts deposited on slides were
642 permeabilized with 0.2% Triton X-100 in PBS, washed and labeled with an affinity purified rat
643 anti-TgIMC3 antibody (1:250 dilution in PBS with 3%BSA for 1 hour at room temperature).
644 Following 3 PBS washes slides were labeled with goat anti-rat conjugated with Oregon Green
645 (1:2000, Molecular Probes/ Thermo) and Hoescht dye (300nM, Molecular Probes/ Thermo).
646 Stained tissue cysts were sealed under a coverslip using MOWIOL prior to imaging. Staining
647 of the tissue cyst wall was performed using FITC-conjugated Dolichos biflorus lectin (DBA,
648 Vector Laboratories) at a 1:2000 dilution.
649
650 **Amyloglucosidase digestion:** Glass slide with deposited purified tissue cysts were washed
651 thrice in 1X citric acid buffer (100mM citric acid/ 100mM dibasic sodium citrate sesquihydrate
652 pH4.6- Sigma) in a Coplin jar. 10 or 25 units of Amyloglucosidase from *Asperigillus niger* (EC-
653 232-844-2)(Megazyme, E-AMGDF, cat# A7096) enzyme were diluted in 1X citric acid buffer
654 and transferred directly onto the site of the deposited tissue cysts onto the glass slide with the
655 region containing tissue cysts outlined using a wax pencil. The control slides were treated with
656 1X citric acid buffer. Both control and test slides were incubated at room temperature overnight
657 in a tightly sealed, moist chamber. The slides were washed 10 times in 1X PBS++ (PBS with
658 0.5mM Ca/Mg) buffer in a Coplin jar and processed for PAS and DAPI staining prior to imaging.
659
660 **Image acquisition and analysis:** The images were acquired on a Zeiss AxioVision upright
661 microscope using a 100X 1.4NA oil immersion objective. Images were acquired as Z-stacks
662 centered around the center of the imaged tissue cyst, using a Zeiss AxioCam MRM digital
663 camera using Zeiss Zen software to control both the camera and motorized stage. The number

664 of Z-stacks acquired was dependent on the size of the thickness of the tissue cyst being imaged
665 although the height of the z-interval was kept constant at 0.24 μm. Acquisition of discrete
666 entities (nuclei, mitochondria and TgIMC3 scaffolds) were subjected to deconvolution using
667 the iterative algorithm in the Zeiss Zen software. For the quantification of PAS staining
668 deconvolution of the signal was not used as the application of the software artificially
669 "normalized" the signal intensity by preferentially exaggerating weak signals thereby reducing
670 the dynamic range. Images in all channels (DAPI-blue, TgIMC3-FITC-green, and PAS-Texas
671 Red were acquired as co-registered grayscale images using fixed exposure times that were
672 empirically determined to provide the optimal signal to noise profile for each channel
673 independently. As PAS treatment was observed to affect the detection of TgIMC3 (**Suppl S3**),
674 all quantification of TgIMC3 was performed on samples that were not PAS treated. The center
675 slice from the z-stack image of each cyst (either deconvoluted or not) was selected and
676 exported in a TIFF format without compression for further analysis. The cyst images with an
677 even number of slices in the Z stack, the slice below the center, were selected. Quantification
678 of AG levels based on PAS staining using AmyloQuant was performed as below with the
679 workflow outlined in **Figure 3B**. Quantification of TgIMC3 intensity within individual tissue cysts
680 was established using Image J as described previously (5).
681
682 **Packing density:** Tissue cysts were co-stained with DAPI, and DBA-FITC was used to label
683 the bradyzoites nucleus and highlight the cyst periphery by labeling the cyst wall. The cyst
684 diameter was determined in Fiji (NIH-Image J) by drawing the ROI around the cyst, using DBA
685 staining as the reference. The Multi-point counter mark and count feature in NIH-Image J was
686 used to manually count nuclei within the imaged volume. Once the value of cyst diameter and
687 total nucleus was obtained, packing density was calculated using the formula describing this
688 calculation is $PD = N / (\pi r^2 \times h)$, where PD=packing density, N = # of bradyzoites/ nuclei, r =
689 cyst radius, h=height of selected slices which is constant (0.24 μm), and represents the z-stack
690 interval.

Statistical Analyses: Statistical analyses were performed using GraphPad with specific tests applied in the figure legends.

Development of AmyloQuant

The images for AG analyses were processed using the following algorithm. From the 8-bit grayscale image AGo, first, a modified Otsu threshold (34) for intensity (to) was obtained, the threshold was scaled by a factor (<1), and the scaled threshold was used to binarize the image. The binary image and "region props" function in Matlab was used to detect the boundary of the cyst. This boundary generated a circular mask delineating the region of interest (ROI). The detected ROI was visualized, and a manual correction factor α (selected via the user interface) was applied, αROI (making the ROI larger or smaller) when necessary. The original grayscale image AG_o was multiplied by the mask to set all pixels outside of the ROI to zero, and then the image was segmented into 4 binary images using three pre-defined intensity cutoffs, i_m, i_l, and i_b as follows: AG_h was computed from AG_o using a condition that all pixels within AG_o with intensity values ≥ i_m were set equal to 1 and all pixels with intensities < i_m were set to be 0. Likewise, AGm was computed by setting all pixels with intensities ≥ il and <im to be equal to 1 and the rest equal to 0 and for AGl, the pixels with intensities ≥ ib and <il was set equal to 1, and the rest were set to 0. All pixels within the ROI with intensities <i_b were set to be equal to 1 and others to be 0 to generate AG_b. The total number of pixels with values equal to 1 were counted within each of the four images to generate counts k_h, k_m, k_l, and k_b. These counts were then normalized by k_t, the total number of pixels within the ROI, e.g., k sub h over k sub t, and expressed as a percent fraction of the image intensity within each of the four intensity ranges.

$AG_h(x,y) = 1$ if $AG_o(x,y) \geq i_m$ else $AG_h(x,y) = 0$

$AG_m(x,y) = 1$ if $i_l \leq AG_o(x,y) < i_m$ else $AG_m(x,y) = 0$

$AG_l(x,y) = 1$ if $i_b \leq AG_o(x,y) < i_l$ else $AG_l(x,y) = 0$

$AG_b(x,y) = 1$ if $AG_o(x,y) < i_b$ else $AG_b(x,y) = 0$

716 The user interface for the program includes a slider labeled 'Scale ROI,' which allows for the selection
717 of the α value, allowing for adjustments ranging from 90% to 110% of the automatically detected ROI.
718 The pre-defined intensity cutoffs of i_b, i_l, i_m are input into the 'Background thresh,' 'Low thresh,' and
719 'Moderate thresh' fields, respectively (**Fig. 3A**). The pixels present within the ROI can be visualized in
720 the histogram displayed along with vertical lines representing the cutoffs used. The 4 binary images
721 created are merged into a single image showing all low-intensity pixels in blue, moderate-intensity
722 pixels in green, and high-intensity pixels in red, with the background being black. The percent fraction
723 of the intensities within each of the four intensity ranges and the total number of pixels within the ROI
724 are displayed. The code for the application was developed using Matlab.

725

726 **Acknowledgements:**

727 The authors acknowledge the support and assistance of the staff of the vivarium from the
728 Department of Animal Laboratory Medicine at the University of Kentucky. We thank Drs
729 Matthew Gentry and Matthieu Colpaert for their insights regarding amylopectin metabolism and
730 dynamics. This work is supported by grants from the US National Institutes of Health
731 RO1AI145335 (to AP and APS) and R21 AI150631 awarded to APS. RDM was supported by
732 GRFP 1247392 from the NSF.

733

734 **Author Contributions:**

735 Conceptualization (AT, AP and APS), Methodology (AT, JSM, AP and APS), Formal analysis
736 (AT, JSM, RWD, RDM, AP and APS), Investigation (AT, JSM, RWD, RDM, AP and APS),
737 Writing- original draft (AT, APS), Writing-review and editing (all authors), Visualization (AT, JSM,
738 AP, APS), Project administration (APS), Funding acquisition (AP, APS).

739

740 **Conflicts of Interest**: None

741 **Figure Legends:**

742 **Figure 1. Heterogenous distribution of amylopectin granules within encysted**
743 **bradyzoites in vivo.** (**A**) Amylopectin is an α1,4-linked linear glucose polymer connected with
744 α1,6 branched linkages. (**B**) Steady state levels of amylopectin in water insoluble
745 stach/amylopectin granules (AG) are dictated by the balance between amylopectin synthesis
746 and turnover. Enzymatic activities promoting synthesis include hexokinase (HK),
747 phosphoglucomutases (PGM1/2), UDP-dependent glucose 1 phosphatase
748 (UGPase/AGPase), the commitment step for starch synthesis, Starch/Glycogen synthase
749 (Synthase) and Branching enzyme (BE). Upon synthesis branched amylopectin polymer
750 chains wind expelling water to from the water insoluble starch/ amylopectin granules.
751 Degradation of amylopectin begins with the phosphorylation of the glucose moiety to unwind
752 the amylopectin chain by a glucan kinase allowing access of amylase to the unwound starch
753 molecule releasing glucose. Amylase activity is blocked at sites of glucan phosphorylation
754 necessitating a glucan phosphatase to assure continued degradation. (**C**) PAS and
755 hematoxylin-stained mouse brain histology showing encysted bradyzoites with variability in the
756 distribution of amylopectin. Amylopectin within bradyzoites is evident with the pink stain.
757 Variability of AG within the same cyst and across cysts is evident. Bradyzoite clusters with low
758 levels of amylopectin within the cyst are encircled with a dashed yellow line. (*Scale bar, 10μm*).

759

760 **Figure 2. Amylopectin levels are not defined by tissue cyst size.**
761 (**A**) Tissue cysts were designated as small (<30μm diameter), medium sized (30-60μm
762 diameter or large (>60μM diameter). Representative images of PAS intensity, defining low,
763 mean and high ranges in cysts of each size class. PAS intensity is in grayscale values
764 determined from the captured grayscale image. Scale bar = 10μm. (**B**) The relationship
765 between cyst size and mean PAS intensity for 180 tissue cysts (30x6) acquired at random at

766 6 weekly time points from week 3-8 post infection. Of the 180 tissue cysts 38 (21%) were
767 small, 118 (66%) were medium sized and 24 (13%) were large. Tissue cysts in this data set
768 were analyzed by week in Figures 4,5. While a trend line (r2 = 0.0562) suggest a weak
769 correlation between cyst size and AG levels based on PAS intensity.
770 Pearson Coefficient = -0.236.

771 **Figure 3. Implementation and validation of AmyloQuant and optimization of PAS**
772 **labeling.** AmyloQuant is an intensity-based image analysis tool that analyzes the
773 heterogeneity in amylopectin distribution in tissue cysts**.** (**A,B**) The AmyloQuant application
774 allows for the establishment of a region of interest (tissue cyst) within which the distribution of
775 PAS intensity is plotted. The application allows for the setting of 3 threshold cutoffs defining 4
776 intensity bins, 1. Background (BG-black), Low intensity (Blue), Moderate/Intermediate (Int)
777 intensity (Green) with values above the moderate threshold defining the high intensity pixels
778 (red). The total recorded pixels and proportions in each of the 4 bins is established and a
779 spatial color-coded heat map generated for each cyst. (**C**) Optimization of PAS staining of
780 tissue cyst for analysis. The Schiff reagents in PAS staining were diluted with tap water in a
781 1:4 (standard protocol), 1:10, and 1:20 ratio. All the images are captured at the same exposure
782 conditions. The top panel shows the cyst image and their respective heatmap from
783 AmyloQuant analysis. Based on the PAS intensity of the image, a 1:10 ratio is selected as the
784 optimum condition. (**D**) Validation of AmyloQuant sensitivity. A PAS-stained cyst was imaged
785 at varying exposure times and analyzed using AmyloQuant with identical threshold values for
786 the pixel bins (BG thresh-10/ Low thresh-25/ High thresh-50). Longer exposure times result in
787 brighter which is reflected in the AmyloQuant generated spatial heat maps. The 1 second
788 exposure was selected as optimal with the optimized PAS staining conditions. (**E**) Acid-Alpha-
789 Glucosidase targets both the linear α1,4 and branched α1,6 glucan linkages resulting in the
790 breakdown of amylopectin. (**F**) The specificity of PAS staining for amylopectin is validated by
791 enzymatic digestion of issue cysts with 10 and 25 units of Acid-Alpha-Glucosidase as is evident

792 from both the intensity following PAS labeling and is captured by the AmyloQuant generated
793 spatial heat map. The control sample was incubated only with a buffer without the addition of
794 acid alpha glucosidase. (*scale bars*,10μm).

795 **Figure 4. Amylopectin dynamics in the early phase of the chronic infection.** PAS stained
796 images of thirty randomly acquired tissue cysts from mice infected for 3 (A,B,C,D), 4 (E,F,G,H)
797 and 5 (I,J,K,L) weeks were analyzed using AmyloQuant. The background (black: 0-10), low
798 (blue:10-25), moderate (green: 25-50) threshold values, with the final high (red: >50) bin
799 defining the 4 bins for analysis presented in a stacked plot format. The tissue cysts were
800 ordered based on the level of high (red) intensity pixels, and secondarily in cysts lacking high
801 intensity pixels on level of moderate (green) intensity pixels. In order to capture the diversity of
802 intensity in high range (red: >50), the background thresholds was set at 50 (gray: 0-50) with
803 high range bins expanded to 50-75 (pink), 75-100 (magenta) and >100 (purple) (B,F,J). The
804 pie charts (C,G,K) represent the pixel intensity distribution following aggregation of the tissue
805 cysts analyzed at each time point. The values, represented as a percentage of the total pixels
806 in each of bin, are presented in the accompanying legend. The tissue cysts represented at
807 each time account for 4258 bradyzoites at week 3, 5485 bradyzoites at week 4 and 5946
808 bradyzoites at week 5 respectively. Finally, AmyloQuant generated spatial heat maps are
809 presented as thumbnails for every 5th tissue cyst for each week post infection (D,H,L).
810 Consistent with the accumulation of amylopectin during the course of the chronic infection, we
811 observe as general trend of increased AG with a general increase in the levels of intermediate
812 and high intensity pixels reflected for the population in the pie charts (C, G, K) and spatial heat
813 maps (D, H, L).
814

815 **Figure 5. Amylopectin dynamics with the maturation of the chronic infection.**
816 PAS stained images of thirty randomly acquired tissue cysts from mice infected for 6 (A,B,C,D),
817 7 (E,F,G,H) and 8 (I,J,K,L) weeks analyzed using AmyloQuant. The background (black: 0-10),

818 low (blue:10-25), moderate (green: 25-50) threshold values, with the final high (red: >50) bin
819 defining the 4 bins for analysis presented in a stacked plot format. The tissue cysts were
820 ordered based on the level of high (red) intensity pixels, and secondarily in cysts lacking high
821 intensity pixels on level of moderate (green) intensity pixels. In order to capture the diversity of
822 intensity in high range (red: >50), the background thresholds was set at 50 (gray: 0-50) with
823 high range bins expanded to 50-75 (pink), 75-100 (magenta) and >100 (purple) (B,F,J). The
824 pie charts (C,G,K) represent the pixel intensity distribution following aggregation of the tissue
825 cysts analyzed at each time point. The values, represented as a percentage of the total pixels
826 in each of bin, are presented in the accompanying legend. The tissue cysts represented at
827 each time account for 8407 bradyzoites at week 6, 4347 bradyzoites at week 7 and 6802
828 bradyzoites at week 8 respectively. Finally, AmyloQuant generated spatial heat maps are
829 presented as thumbnails for every 5th tissue cyst for each week post infection (D,H,L). The
830 proportion of tissue cysts with high levels of AG increases dramatically at weeks 6 and 7 (A,B,
831 E, F). This is reflected in the distribution of pixel intensities for the bradyzoite population evident
832 in the pie charts (C,G) as well as within the spatial heat maps generated using AmyloQuant
833 (D,E). The transition from week 7 to week 8 is defined by a profound reduction in AG levels
834 (E,F,I,J) withing individual tissue cysts that is reflected in both the overall distribution of PAS
835 intensities evident in the pie charts (G,K) as well as the spatial heat maps bradyzoite population
836 (H,L).
837
838 **Figure 6 Levels and distribution of active mitochondria based on the membrane**
839 **potential is highly variable across tissue cysts and displays a temporal profile.**
840 **(A)** MitoTracker labeling (red) of freshly isolated ex vivo tissue cysts (DBA-green) reveal
841 considerable heterogeneity ranging from the absence of active mitochondrial to cysts with a
842 high level of activity (left panel). Most tissue cysts display a patchwork of activity as observed
843 in the overlay of the MitoTracker (red) and DIC image (right panel). Nuclei are labeled with
844 DAPI (blue). (**B)** The proportion of active mitochondria relative to nuclei in tissue cysts

845 harvested weekly from week 3 to 8 post infection show a trend of increasing activity from weeks
846 3-6 followed by a large increase in the number of cysts with >95% of active mitochondria
847 relative to nuclei at week 7. A broad distribution is re-established at week 8 post infection. In
848 instances where the number of mitochondrial profiles exceeded the number of nuclei within the
849 cyst the value was corrected to 100%. Mitochondrial profiles exceeding the number of nuclei
850 could be due to documented fragmentation of the organelle. 1 cyst out of 33 at week 6, 12
851 cysts out of 39 at week 7 and 2 cysts out of 34 at week 8 were subject to correction. Statistical
852 analysis performed using one-way ANOVA with Tukey's multiple comparisons test. A *: 0.021-
853 0.030 p-value.

854 **Figure 7. Amylopectin influences the replication of bradyzoites within tissue cysts.** (**A**)
855 Recently replicated bradyzoites within tissue cysts can be identified by the intensity of TgIMC3
856 labeling. The mean intensity of tissue cysts harvested from weeks 3-8 was measured using
857 Image J. The brightest, mean intensity and dimmest cyst at each timepoint Tissue cysts
858 harvested weekly from week 3-8 are represented as a measure of relative mean intensity. All
859 images were captured using identical exposure parameters. Images represent the center slice
860 of a z-stack (z interval of 0.24μm) following iterative deconvolution. Scale bar represents 10
861 microns. (**B**) Distribution of mean TgIMC3 intensities in tissue cysts harvested at weeks 3-8
862 reveal an overall pattern of reducing recent replicative activity during the early phase of the
863 chronic infection (week 3-5) that is followed by a burst of recent replication within tissue cysts
864 in the latter half of the cycle (weeks 6-8). Data represent sample means for week 3 (n=35
865 cysts), week 4 (n=40), week 5 (n=35), week 6 (n=34), week 7 (n=37) and week 8 (n= 37).
866 Statistical Analysis: One way ANOVA with Tukeys multiple comparisons test. Adjusted p
867 values: *: 0.011, **: 0.002, ***: 0.0002, ****: <0.0001 (**C**) The packing density, a measure of
868 cyst occupancy was determined for the TgIMC3 labeled cysts. Packing densities revealed a
869 generally stable pattern from week 3-7 consistent with balanced sporadic intracyst replication.
870 The transition from week 7 to week 8 was noted by extensive intra-cyst bradyzoite replication

871 within most tissue cysts indicative of a coordinated replicative burst. Statistical analysis: One
872 way ANOVA with Tukey's multiple comparisons test. Adjusted p values: **: 0.0030, ***: 0.0007,
873 ****: < 0.0001.

874 **Figure 8**. **Correlation of AG dynamics, mitochondrial activity, recency of replication and**
875 **packing density follow distinct patterns**. **Panel 1**: Mean PAS intensity for the analyzed
876 tissue cyst populations harvested weekly from week 3-8 post infection reveal a slow increase
877 in the early phase (weeks 3-5) followed by rapid accumulation of AG (weeks 6-7) and
878 subsequent loss at week 8. (Dashed line +/- SEM) **Panel 2**: This pattern is largely mirrored by
879 the proportion of active mitochondria with the increased levels of active mitochondria initiating
880 at week 4, peaking at week 7 post infection. This is followed by a precipitous drop between
881 weeks 7-8 resetting a potential cycle. **Panel 3**: Recency of replication based on mean TgIMC3
882 intensity reveals a shutting down of active replication between weeks 3-5 a period associated
883 with limited AG accumulation. Increases in AG accumulation at weeks 6-8 are associated with
884 a marked increase (week 6-7) of recent replicative activity that is sustained at week 8. **Panel**
885 **4:** A general trend for a stable packing density between weeks 3 and 8 is consistent with
886 balanced cyst expansion matched with sporadic growth. The transition from week 7 to 8 is
887 associated with coordinated intracyst replication that is accompanied by the depletion of AG
888 reserves and overall mitochondrial activity. Statistical analyses: In each case the dashed line
889 represents the boundary of the standard error of the mean (+/- SEM).

890 **Supplemental Data Figure Legends**

891 **Supplemental Figure 1. Effect of AmyloQuant threshold value settings on the**
892 **distribution of PAS intensities.** Application of distinct threshold values in AmyloQuant in the
893 same tissue cyst image (original images are adjusted) results in a fundamentally different
894 patterns to define the backroad, low, intermediate and high bins thus impacting the
895 representation of AG distribution. The optimized setting (Intermediate) of the threshold value

896 provided the most balanced representation for typical tissue cysts. Thumbnails below the
897 intensity histograms present the AmyloQuant generated heat maps for each of the threshold
898 setting presented here.

899 **Supplemental Figure S2. Amylopectin dynamics revealed in methanol fixed tissue cyst**
900 **following PAS staining and analysis in AmyloQuant** analysis of tissue cysts fixed in
901 methanol. The bar graphs represent the ordered distribution of intensities in the background,
902 low, intermediate and high ranges following the setting of bins at : BG: 0-10 (black), Low10-25
903 (blue), Intermediate 25-50 (green) and high >50 (red). The heatmaps under each set of bar
904 graphs represent AmyloQuant generated spatial distributions of the 30 tissue cysts at 5 cyst
905 intervals. While the overall AG pattern from week 3-8 is identical to that observed for PAS
906 labeling of over this temporal course, a significant loss of signal is evident for methanol fixed
907 tissue cysts. The amylopectin distribution pattern in chronic infection's early and late phases is
908 similar to the PFA fixed and unaffected, irrespective of the fixation condition.

909 **Supplemental Figure S3. Interference of PAS staining with TgIMC3 labeling. (A)** Counter
910 staining of PAS stained tissue cysts affected the efficiency of TgIMC3 labeling. In general poor
911 TgIMC3 staining was noted in tissue cysts with high PAS labeling. Scale bar represents 10 μm.
912 (**B**) Head to head comparison of TgIMC3 labeling on both untreated (-PAS) and PAS treated
913 (+PAS) tissue cysts shows no difference at time points with low AG (week 3 and 8), but
914 significant PAS dependent differences in TgIMC3 labeling at time points associated with higher
915 levels of AG and thus higher PAS binding. Statistical Analysis: One way ANOVA with Mann-
916 Whitney Test. P values: ns: not significant, **: 0.0047, ****= < 0.0001.

917

918 **Supplemental Figure S4. PAS staining impacts the quality of DAPI labeling**
919 **compromising the ability to accurately count nuclei**. (**A**) PAS labeling of PFA and methanol
920 (not shown) fixed tissue cysts affected the integrity and quality of nuclear staining that resulted

921 in differentially diffuse nuclear profiles. While not uniform, the effect on PAS on nuclear staining
922 was markedly more pronounced in tissue cysts from time points associated with higher levels
923 of AG and thus PAS labeling. Additional factors leading to the exclusion of tissue cysts for
924 analysis included non circular cysts and clearly damaged broken cysts. These issues
925 precluded the accurate demarcation of the whole tissue cyst in AmyloQuant affecting the
926 accuracy of both PAS and nuclear quantification. (**B**) The proportion of PAS/DAPI co-stained
927 tissue cysts within which the number of nuclei could not be accurately counted was significantly
928 greater at time points associated with high PAS labeling (weeks 5-7). For this reason,
929 measurements relating to the packing density which is dependent in the accuracy of the
930 nuclear count was performed on non-PAS staining tissue cyst from the same cohort at each
931 time point. Damage to nuclei is likely connected to the low pH associated with deposited Schiff
932 periodic acid dye in an AG concentration dependent manner.

933

934

935

936

937 **Literature Cited**

938 1. J. P. Dubey, J. L. Jones, *Toxoplasma gondii* infection in humans and animals in the United
939 States. *International journal for parasitology* **38**, 1257-1278 (2008).
940 2. D. E. Hill, S. Chirukandoth, J. P. Dubey, Biology and epidemiology of *Toxoplasma gondii*
941 in man and animals. *Anim Health Res Rev* **6**, 41-61 (2005).
942 3. A. P. Sinai *et al.*, Reexamining Chronic *Toxoplasma gondii* Infection: Surprising Activity
943 for a "Dormant" Parasite. *Curr Clin Microbiol Rep* **3**, 175-185 (2016).
944 4. J. P. Dubey, D. S. Lindsay, C. A. Speer, Structures of *Toxoplasma gondii* tachyzoites,
945 bradyzoites, and sporozoites and biology and development of tissue cysts. *Clin Microbiol*
946 *Rev* **11**, 267-299 (1998).
947 5. E. Watts *et al.*, Novel Approaches Reveal that *Toxoplasma gondii* Bradyzoites within
948 Tissue Cysts Are Dynamic and Replicating Entities In Vivo. *mBio* **6**, e01155-01115 (2015).
949 6. V. Tu, R. Yakubu, L. M. Weiss, Observations on bradyzoite biology. *Microbes and infection*
950 */ Institut Pasteur* **20**, 466-476 (2018).
951 7. T. V. Beyer, C. Siim, W. M. Hutchison, [Cytochemical study of different stages in the life
952 cycle of *Toxoplasma gondii*. I. Amylopectin and lipids in endozoites]. *Tsitologiia* **19**, 681-
953 685 (1977).
954 8. A. Coppin *et al.*, Developmentally regulated biosynthesis of carbohydrate and storage
955 polysaccharide during differentiation and tissue cyst formation in *Toxoplasma gondii*.
956 *Biochimie* **85**, 353-361 (2003).
957 9. A. Coppin *et al.*, Evolution of plant-like crystalline storage polysaccharide in the protozoan
958 parasite *Toxoplasma gondii* argues for a red alga ancestry. *J Mol Evol* **60**, 257-267 (2005).
959 10. Y. Guerardel *et al.*, Amylopectin biogenesis and characterization in the protozoan parasite
960 *Toxoplasma gondii*, the intracellular development of which is restricted in the HepG2 cell
961 line. *Microbes and infection / Institut Pasteur* **7**, 41-48 (2005).
962 11. L. Lim, G. I. McFadden, The evolution, metabolism and functions of the apicoplast. *Philos*
963 *Trans R Soc Lond B Biol Sci* **365**, 749-763 (2010).

964 12. S. Ball, C. Colleoni, U. Cenci, J. N. Raj, C. Tirtiaux, The evolution of glycogen and starch
965 metabolism in eukaryotes gives molecular clues to understand the establishment of plastid
966 endosymbiosis. *J Exp Bot* **62**, 1775-1801 (2011).
967 13. L. M. Weiss, K. Kim, The development and biology of bradyzoites of *Toxoplasma gondii*.
968 *Front Biosci* **5**, D391-405 (2000).
969 14. D. J. Ferguson, Use of molecular and ultrastructural markers to evaluate stage conversion
970 of *Toxoplasma gondii* in both the intermediate and definitive host. *International journal for*
971 *parasitology* **34**, 347-360 (2004).
972 15. D. J. Ferguson, W. M. Hutchison, An ultrastructural study of the early development and
973 tissue cyst formation of *Toxoplasma gondii* in the brains of mice. *Parasitology research*
974 **73**, 483-491 (1987).
975 16. P. J. Stoward, Studies in fluorescence histochemistry. II. The demonstration of periodate-
976 reactive mucosubstances with pseudo-Schiff reagents. *J R Microsc Soc* **87**, 237-246
977 (1967).
978 17. R. D. Murphy *et al.*, The *Toxoplasma* glucan phosphatase TgLaforin utilizes a distinct
979 functional mechanism that can be exploited by therapeutic inhibitors. *The Journal of*
980 *biological chemistry* **298**, 102089 (2022).
981 18. P. L. Keeling, A. M. Myers, Biochemistry and genetics of starch synthesis. *Annu Rev Food*
982 *Sci Technol* **1**, 271-303 (2010).
983 19. E. V. Quach *et al.*, Phosphoglucomutase 1 contributes to optimal cyst development in
984 *Toxoplasma gondii*. *BMC Res Notes* **15**, 188 (2022).
985 20. S. Saha, B. I. Coleman, R. Dubey, I. J. Blader, M. J. Gubbels, Two Phosphoglucomutase
986 Paralogs Facilitate Ionophore-Triggered Secretion of the *Toxoplasma* Micronemes.
987 *mSphere* **2** (2017).
988 21. P. Chen *et al.*, Key roles of amylopectin synthesis and degradation enzymes in the
989 establishment and reactivation of chronic toxoplasmosis. *Anim Dis* **3** (2023).

990 22. C. Lyu *et al.*, Role of amylopectin synthesis in *Toxoplasma gondii* and its implication in
991 vaccine development against toxoplasmosis. *Open Biol* **11**, 200384 (2021).
992 23. M. Stitt, S. C. Zeeman, Starch turnover: pathways, regulation and role in growth. *Curr Opin*
993 *Plant Biol* **15**, 282-292 (2012).
994 24. J. Compart, A. Apriyanto, J. Fettke, Glucan, water dikinase (GWD) penetrates the starch
995 granule surface and introduces C6 phosphate in the vicinity of branching points.
996 *Carbohydr Polym* **321**, 121321 (2023).
997 25. M. Hejazi *et al.*, Glucan, water dikinase phosphorylates crystalline maltodextrins and
998 thereby initiates solubilization. *Plant J* **55**, 323-334 (2008).
999 26. M. S. Gentry *et al.*, The phosphatase laforin crosses evolutionary boundaries and links
1000 carbohydrate metabolism to neuronal disease. *J Cell Biol* **178**, 477-488 (2007).
1001 27. R. D. Murphy *et al.*, TgLaforin, a glucan phosphatase, reveals the dynamic role of storage
1002 polysaccharides in *Toxoplasma gondii* tachyzoites and bradyzoites. *bioRxiv*
1003 10.1101/2023.09.29.560185 (2023).
1004 28. M. Pan *et al.*, The determinants regulating *Toxoplasma gondii* bradyzoite development.
1005 *Front Microbiol* **13**, 1027073 (2022).
1006 29. T. Sugi, V. Tu, Y. Ma, T. Tomita, L. M. Weiss, *Toxoplasma gondii* Requires Glycogen
1007 Phosphorylase for Balancing Amylopectin Storage and for Efficient Production of Brain
1008 Cysts. *mBio* **8** (2017).
1009 30. A. M. Sullivan *et al.*, Evidence for finely-regulated asynchronous growth of *Toxoplasma*
1010 *gondii* cysts based on data-driven model selection. *PLoS computational biology* **9**,
1011 e1003283 (2013).
1012 31. N. Anghel *et al.*, Endochin-like quinolones (ELQs) and bumped kinase inhibitors (BKIs):
1013 Synergistic and additive effects of combined treatments against Neospora caninum
1014 infection in vitro and in vivo. *Int J Parasitol Drugs Drug Resist* **17**, 92-106 (2021).

1015 32. J. S. Doggett *et al.*, Endochin-like quinolones are highly efficacious against acute and
1016 latent experimental toxoplasmosis. *Proceedings of the National Academy of Sciences of*
1017 *the United States of America* **109**, 15936-15941 (2012).
1018 33. R. S. Vidadala *et al.*, Development of an Orally Available and Central Nervous System
1019 (CNS) Penetrant *Toxoplasma gondii* Calcium-Dependent Protein Kinase 1 (TgCDPK1)
1020 Inhibitor with Minimal Human Ether-a-go-go-Related Gene (hERG) Activity for the
1021 Treatment of Toxoplasmosis. *Journal of medicinal chemistry* **59**, 6531-6546 (2016).
1022 34. N. Otsu, A threshold selection method from gray-level histograms *IEEE Transactions on*
1023 *Systems Man and Cybernetics* **9**, 62-66 (1979).
1024 35. C. A. Troublefield, J. S. Miracle, R. D. Murphy, R. W. Donkin, A. P. Sinai, Factors
1025 Influencing Tissue Cyst Yield in a Murine Model of Chronic Toxoplasmosis. *Infection and*
1026 *immunity* **91**, e0056622 (2023).
1027 36. E. A. Watts, A. Dhara, A. P. Sinai, Purification *Toxoplasma gondii* Tissue Cysts Using
1028 Percoll Gradients. *Curr Protoc Microbiol* **45**, 20C 22 21-20C 22 19 (2017).
1029 37. J. Ovciarikova, L. Lemgruber, K. L. Stilger, W. J. Sullivan, L. Sheiner, Mitochondrial
1030 behaviour throughout the lytic cycle of *Toxoplasma gondii*. *Scientific reports* **7**, 42746
1031 (2017).
1032 38. B. C. Place, C. Troublefield, R. D. Murphy, A. P. Sinai, A. Patwardhan, Computer Aided
1033 Image Processing to Facilitate Determination of Congruence in Manual Classification of
1034 Mitochondrial Morphologies in *Toxoplasma gondii* Tissue Cysts. *Annu Int Conf IEEE Eng*
1035 *Med Biol Soc* **2021**, 3509-3513 (2021).
1036 39. B. C. Place, C. A. Troublefield, R. D. Murphy, A. P. Sinai, A. R. Patwardhan, Machine
1037 learning based classification of mitochondrial morphologies from fluorescence microscopy
1038 images of *Toxoplasma gondii* cysts. *PloS one* **18**, e0280746 (2023).
1039 40. S. W. Perry, J. P. Norman, J. Barbieri, E. B. Brown, H. A. Gelbard, Mitochondrial
1040 membrane potential probes and the proton gradient: a practical usage guide.
1041 *BioTechniques* **50**, 98-115 (2011).

1042 41. F. Seeber, D. J. Ferguson, U. Gross, *Toxoplasma gondii*: a paraformaldehyde-insensitive
1043 diaphorase activity acts as a specific histochemical marker for the single mitochondrion.
1044 *Experimental parasitology* **89**, 137-139 (1998).
1045 42. D. Ghosh, J. L. Walton, P. D. Roepe, A. P. Sinai, Autophagy is a cell death mechanism in
1046 *Toxoplasma gondii*. *Cellular microbiology* **14**, 589-607 (2012).
1047 43. B. Anderson-White *et al.*, Cytoskeleton assembly in *Toxoplasma gondii* cell division.
1048 *International review of cell and molecular biology* **298**, 1-31 (2012).
1049 44. B. R. Anderson-White *et al.*, A family of intermediate filament-like proteins is sequentially
1050 assembled into the cytoskeleton of *Toxoplasma gondii*. *Cellular microbiology* **13**, 18-31
1051 (2011).
1052 45. B. Pfister, S. C. Zeeman, Formation of starch in plant cells. *Cell Mol Life Sci* **73**, 2781-
1053 2807 (2016).
1054 46. P. J. Roach, A. A. Depaoli-Roach, T. D. Hurley, V. S. Tagliabracci, Glycogen and its
1055 metabolism: some new developments and old themes. *The Biochemical journal* **441**, 763-
1056 787 (2012).
1057 47. S. Streb, S. C. Zeeman, Starch metabolism in Arabidopsis. *The Arabidopsis book /*
1058 *American Society of Plant Biologists* **10**, e0160 (2012).
1059 48. A. D. Uboldi *et al.*, Regulation of Starch Stores by a Ca(2+)-Dependent Protein Kinase Is
1060 Essential for Viable Cyst Development in *Toxoplasma gondii*. *Cell host & microbe* **18**,
1061 670-681 (2015).
1062 49. W. Bohne, J. Heesemann, U. Gross, Reduced replication of *Toxoplasma gondii* is
1063 necessary for induction of bradyzoite-specific antigens: a possible role for nitric oxide in
1064 triggering stage conversion. *Infection and immunity* **62**, 1761-1767 (1994).
1065 50. A. V. Naumov *et al.*, Restriction Checkpoint Controls Bradyzoite Development in
1066 *Toxoplasma gondii*. *Microbiol Spectr* **10**, e0070222 (2022).

1067 51. S. S. Lin, U. Gross, W. Bohne, Type II NADH dehydrogenase inhibitor 1-hydroxy-2-
1068 dodecyl-4(1H)quinolone leads to collapse of mitochondrial inner-membrane potential and
1069 ATP depletion in *Toxoplasma gondii*. *Eukaryotic cell* **8**, 877-887 (2009).
1070 52. J. Yang, Z. He, C. Chen, J. Zhao, R. Fang, Starch Branching Enzyme 1 Is Important for
1071 Amylopectin Synthesis and Cyst Reactivation in *Toxoplasma gondii*. *Microbiol Spectr* **10**,
1072 e0189121 (2022).
1073 53. J. Yang *et al.*, *Toxoplasma gondii* alpha-amylase deletion mutant is a promising vaccine
1074 against acute and chronic toxoplasmosis. *Microb Biotechnol* **13**, 2057-2069 (2020).
1075 54. J. L. Wang *et al.*, The protein phosphatase 2A holoenzyme is a key regulator of starch
1076 metabolism and bradyzoite differentiation in *Toxoplasma gondii*. *Nat Commun* **13**, 7560
1077 (2022).
1078 55. M. Zhao *et al.*, PP2Acalpha-B'/PR61 Holoenzyme of *Toxoplasma gondii* Is Required for
1079 the Amylopectin Metabolism and Proliferation of Tachyzoites. *Microbiol Spectr* **11**,
1080 e0010423 (2023).
1081 56. C. W. Vander Kooi *et al.*, From the Cover: Structural basis for the glucan phosphatase
1082 activity of Starch Excess4. *Proceedings of the National Academy of Sciences of the United*
1083 *States of America* **107**, 15379-15384 (2010).
1084 57. C. A. Worby, M. S. Gentry, J. E. Dixon, Laforin: A dual specificity phosphatase that
1085 dephosphorylates complex carbohydrates. *J. Biol. Chem.* **281**, 30412-30418 (2006).
1086 58. Y. Gibon *et al.*, Adjustment of growth, starch turnover, protein content and central
1087 metabolism to a decrease of the carbon supply when Arabidopsis is grown in very short
1088 photoperiods. *Plant Cell Environ* **32**, 859-874 (2009).
1089 59. A. Pokhilko, A. Flis, R. Sulpice, M. Stitt, O. Ebenhoh, Adjustment of carbon fluxes to light
1090 conditions regulates the daily turnover of starch in plants: a computational model.
1091 *Molecular bioSystems* 10.1039/c3mb70459a (2014).
1092 60. A. M. Smith, M. Stitt, Coordination of carbon supply and plant growth. *Plant Cell Environ*
1093 **30**, 1126-1149 (2007).

1094 61. S. Kato, H. G. Nam, The Cell Division Cycle of Euglena gracilis Indicates That the Level
1095 of Circadian Plasticity to the External Light Regime Changes in Prolonged-Stationary
1096 Cultures. *Plants (Basel)* **10** (2021).
1097 62. M. Sasai, M. Yamamoto, Innate, adaptive, and cell-autonomous immunity against
1098 *Toxoplasma gondii* infection. *Exp Mol Med* **51**, 1-10 (2019).
1099 63. M. Sasai, M. Yamamoto, Anti-*Toxoplasma* host defense systems and the parasitic
1100 counterdefense mechanisms. *Parasitol Int* **89**, 102593 (2022).
1101 64. I. A. Khan, S. Hwang, M. Moretto, *Toxoplasma gondii*: CD8 T Cells Cry for CD4 Help.
1102 *Front Cell Infect Microbiol* **9**, 136 (2019).
1103 65. I. A. Khan, M. Moretto, Immune responses to *Toxoplasma gondii*. *Curr Opin Immunol* **77**,
1104 102226 (2022).
1105 66. J. P. Gigley, R. Bhadra, M. M. Moretto, I. A. Khan, T cell exhaustion in protozoan disease.
1106 *Trends in parasitology* **28**, 377-384 (2012).
1107 67. R. Porte *et al.*, Protective function and differentiation cues of brain-resident CD8+ T cells
1108 during surveillance of latent *Toxoplasma gondii* infection. *Proceedings of the National*
1109 *Academy of Sciences of the United States of America* **121**, e2403054121 (2024).
1110 68. M. S. Behnke, J. P. Dubey, L. D. Sibley, Genetic Mapping of Pathogenesis Determinants
1111 in *Toxoplasma gondii*. *Annu Rev Microbiol* **70**, 63-81 (2016).
1112 69. J. P. Dubey, Comparative infectivity of *Toxoplasma gondii* bradyzoites in rats and mice.
1113 *The Journal of parasitology* **84**, 1279-1282 (1998).
1114 70. P. Saraf, E. K. Shwab, J. P. Dubey, C. Su, On the determination of *Toxoplasma gondii*
1115 virulence in mice. *Experimental parasitology* **174**, 25-30 (2017).
1116 71. A. P. Sinai, E. S. Suvorova, The RESTRICTION checkpoint: a window of opportunity
1117 governing developmental transitions in *Toxoplasma gondii*. *Current opinion in*
1118 *microbiology* **58**, 99-105 (2020).

1119 72. C. J. Beckers *et al.*, Inhibition of cytoplasmic and organellar protein synthesis in
1120 *Toxoplasma gondii*. Implications for the target of macrolide antibiotics. *J Clin Invest* **95**,
1121 367-376 (1995).
1122

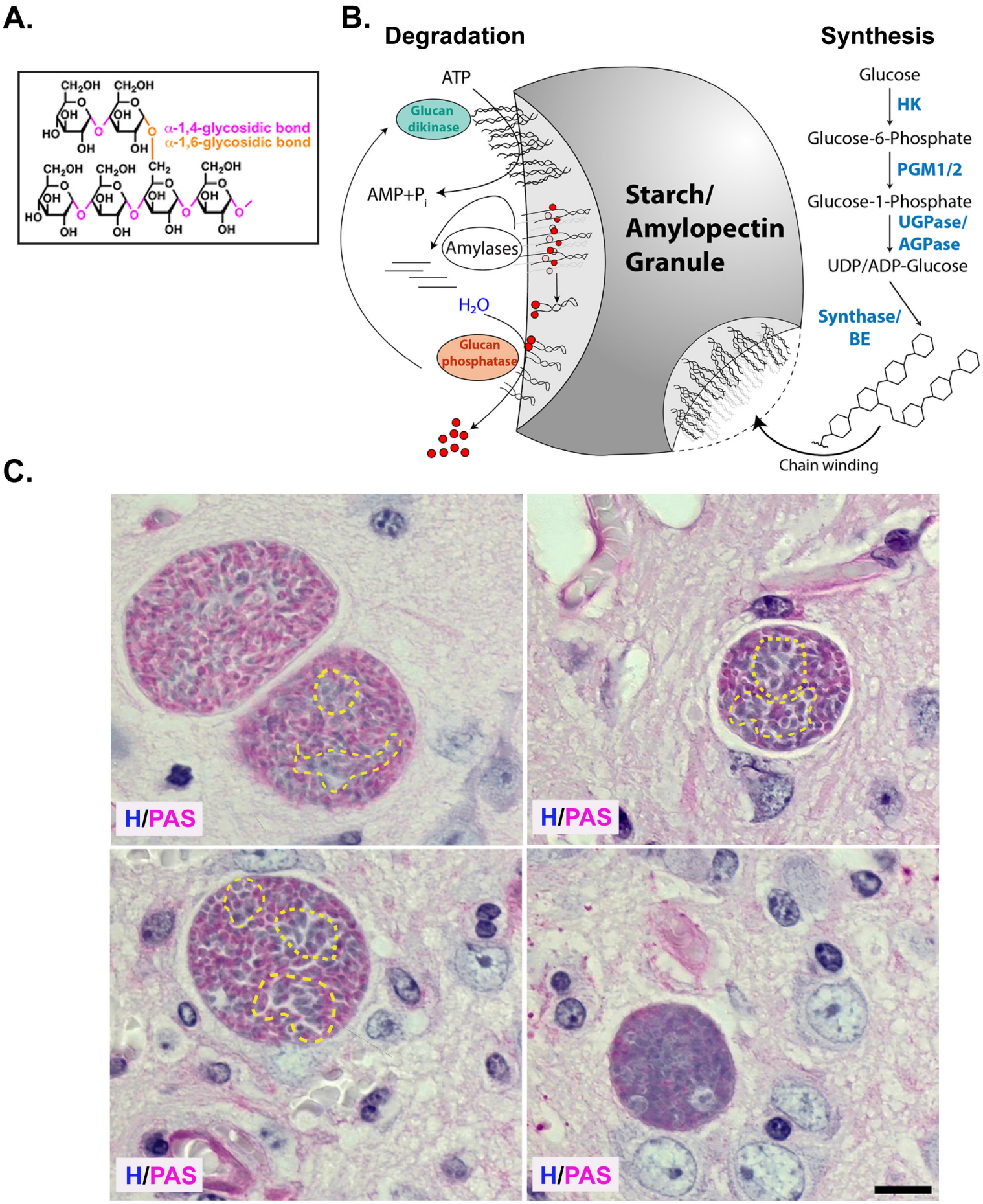

Tripathi et al. 2024 **Figure 1**

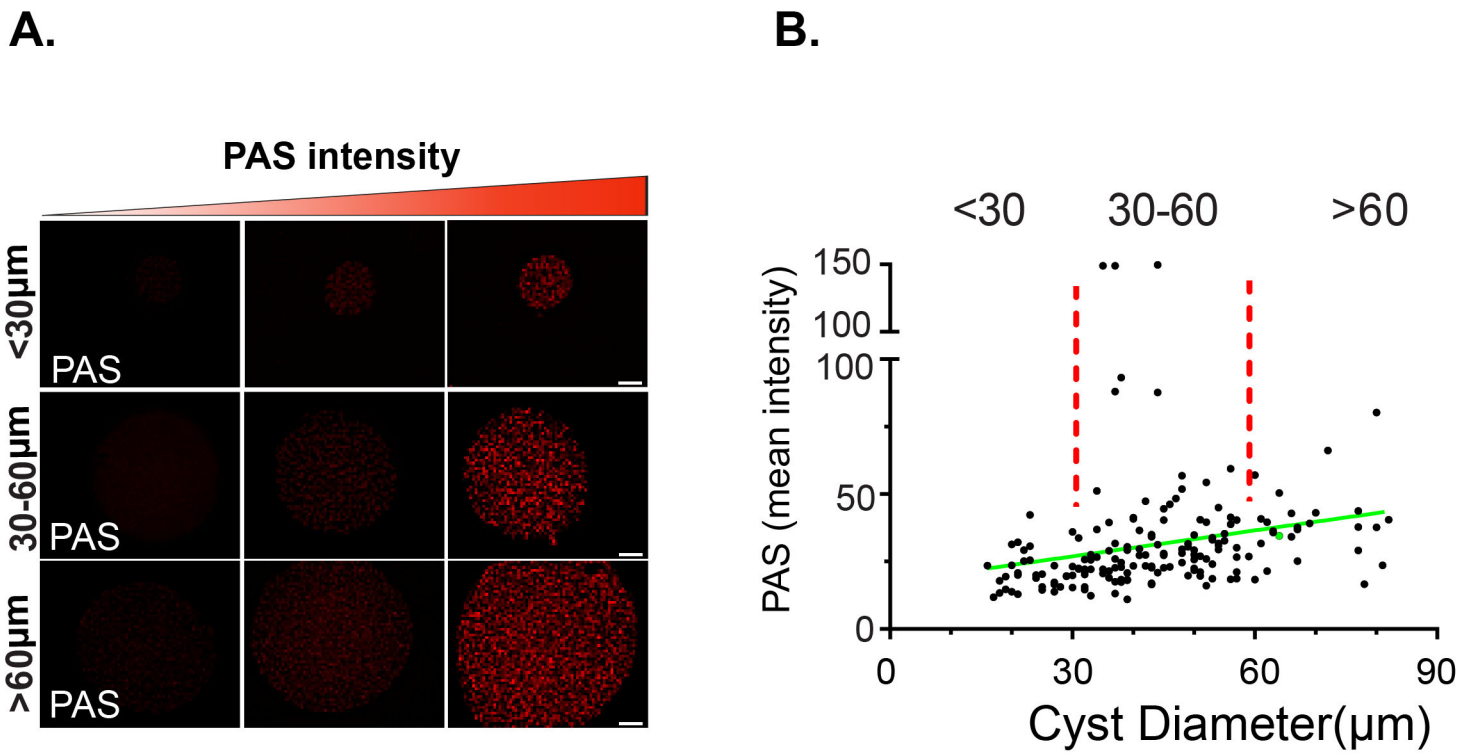

Tripathi et al. 2024 **Figure 2**

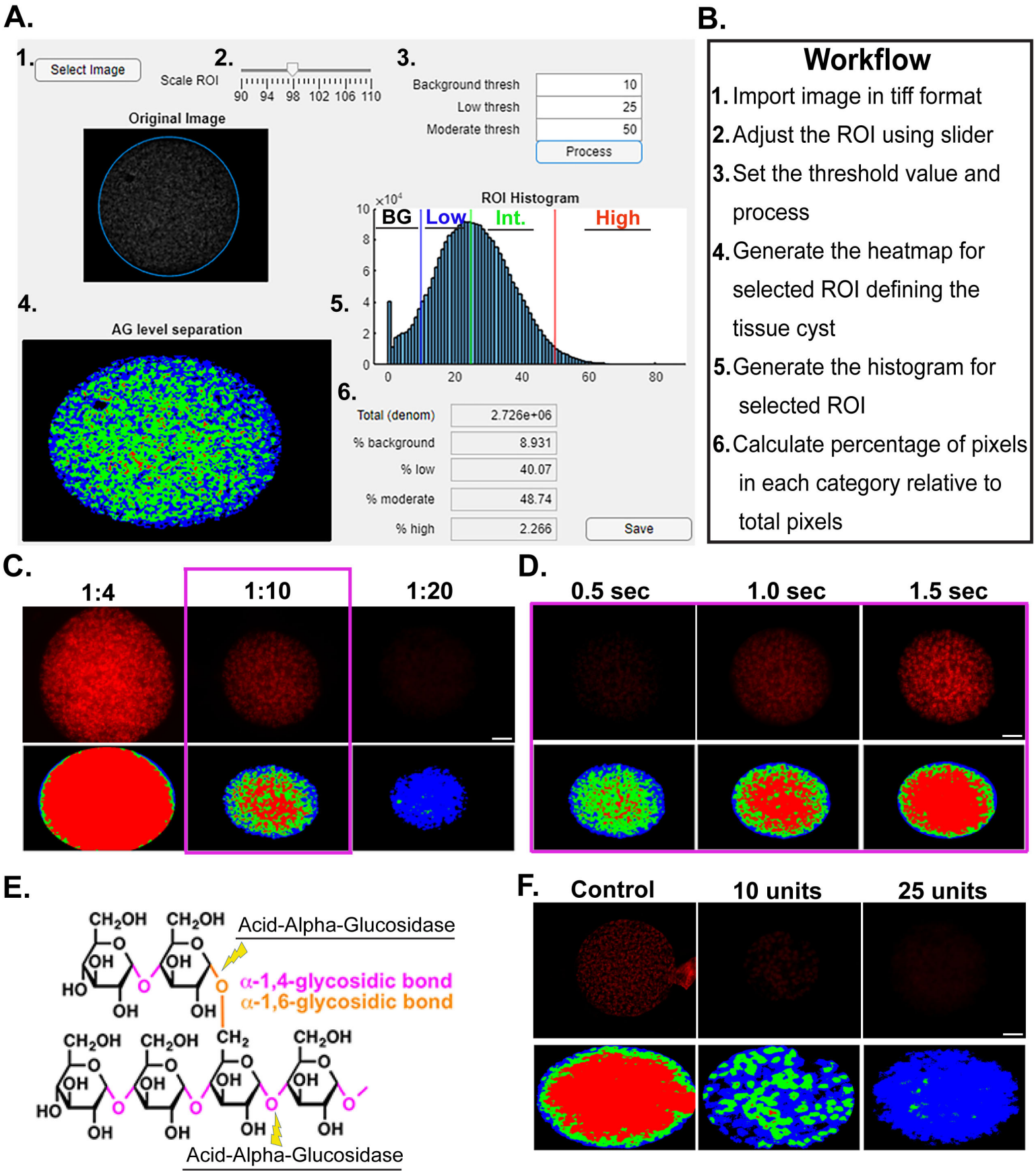

Tripathi et al. 2024 **Figure 3**

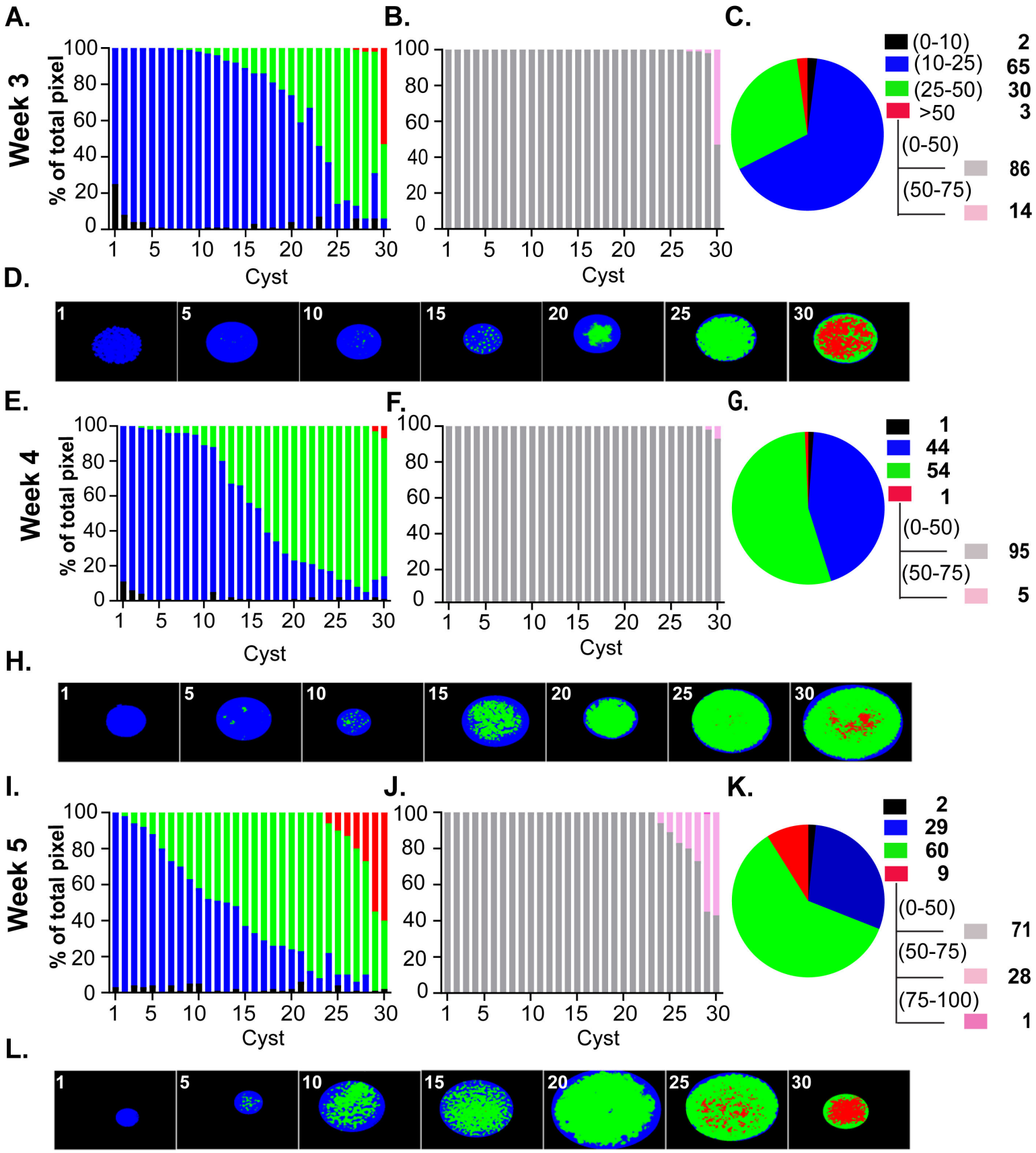

Tripathi et al. 2024 **Figure 4**

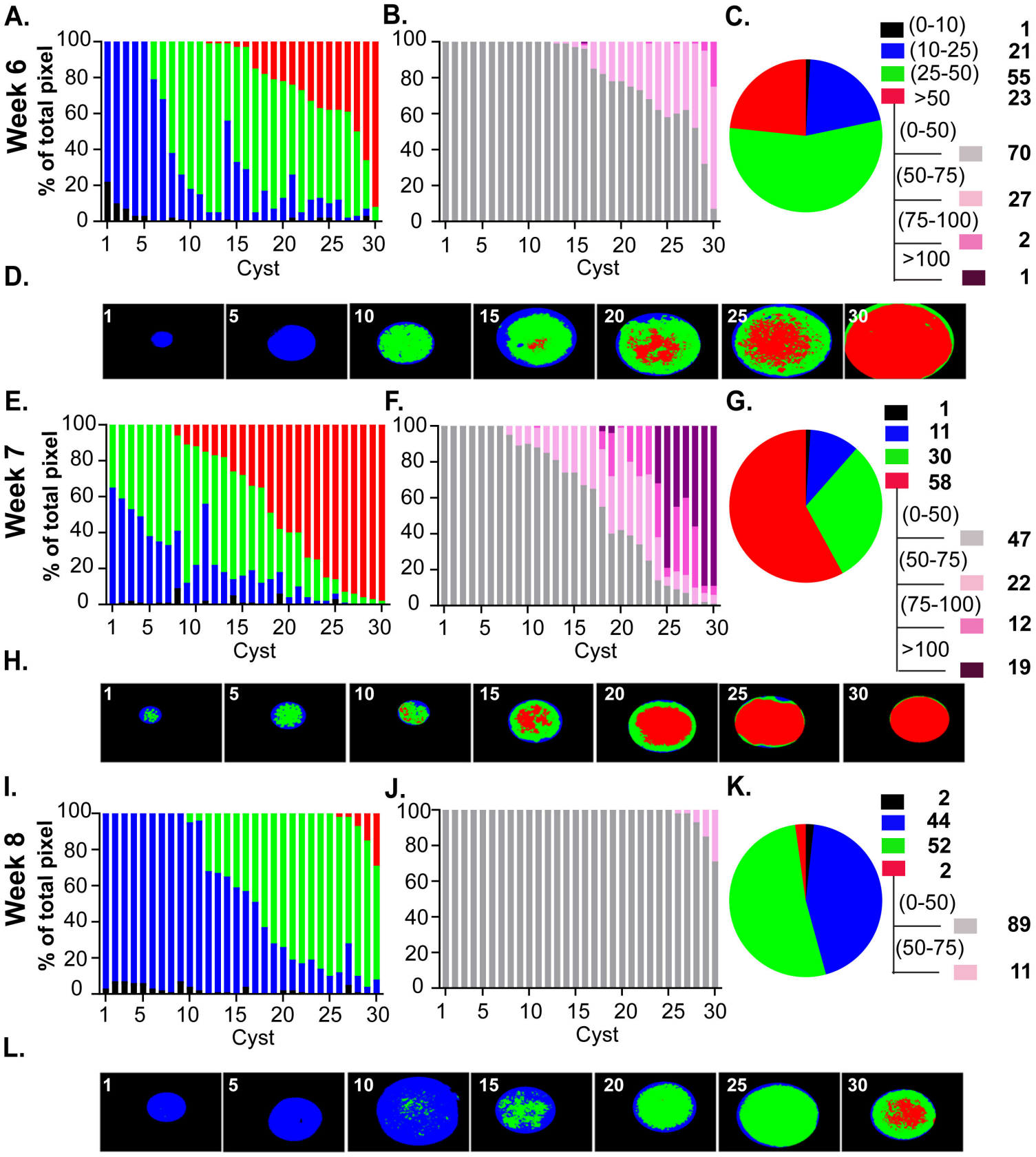

Tripathi et al 2024 **Figure 5**

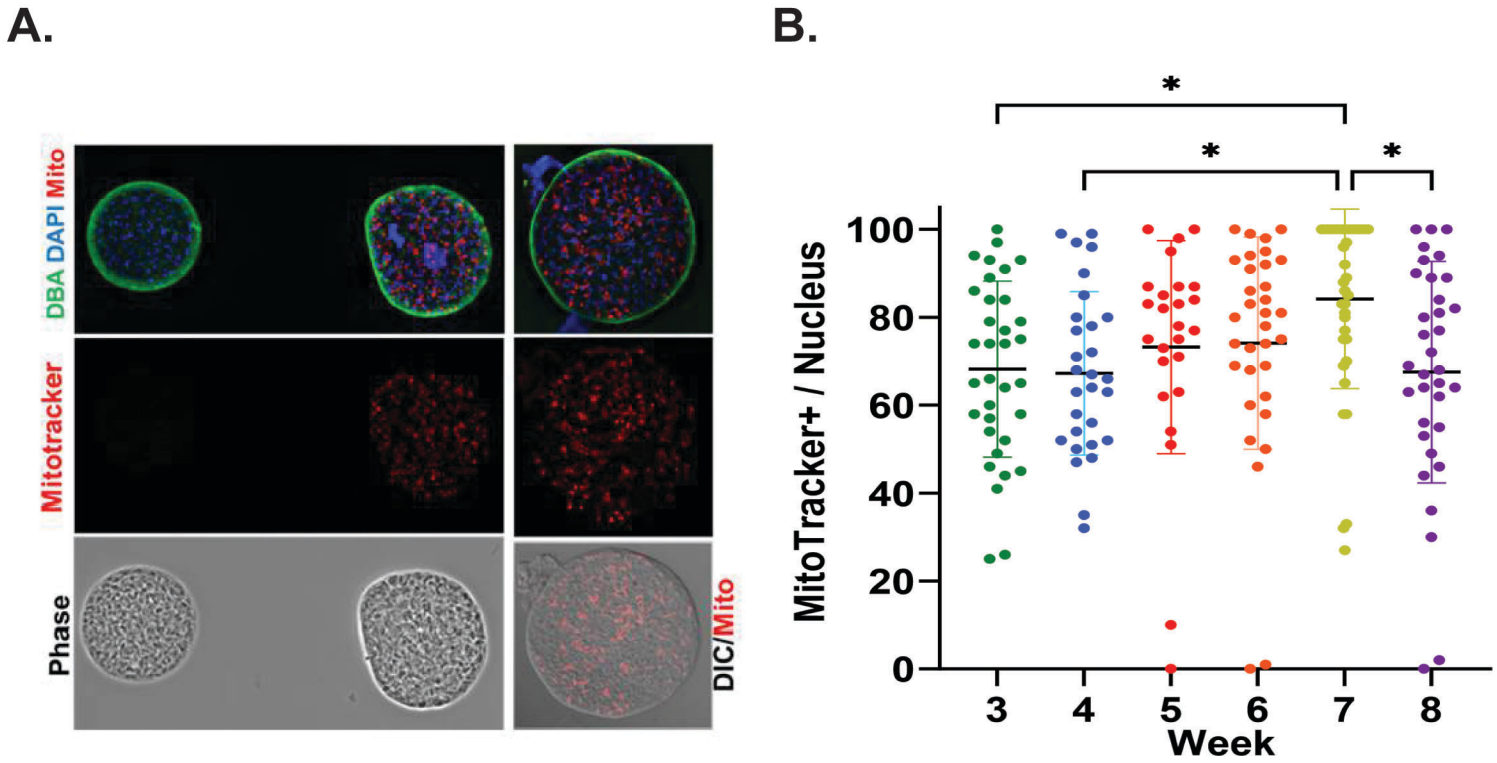

Tripathi et al 2024 **Figure 6**

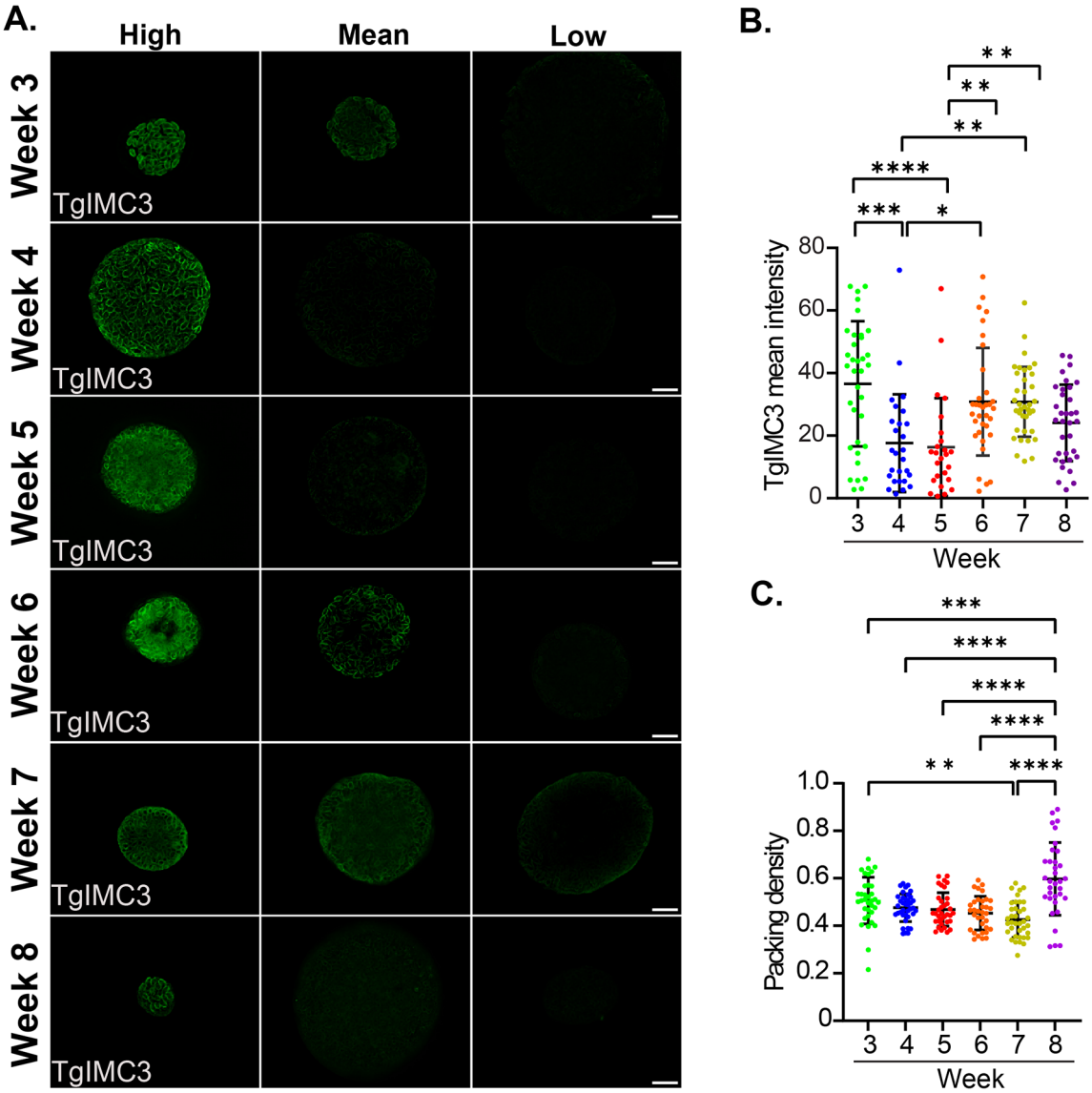

Tripathi et al. 2024 **Figure 7**

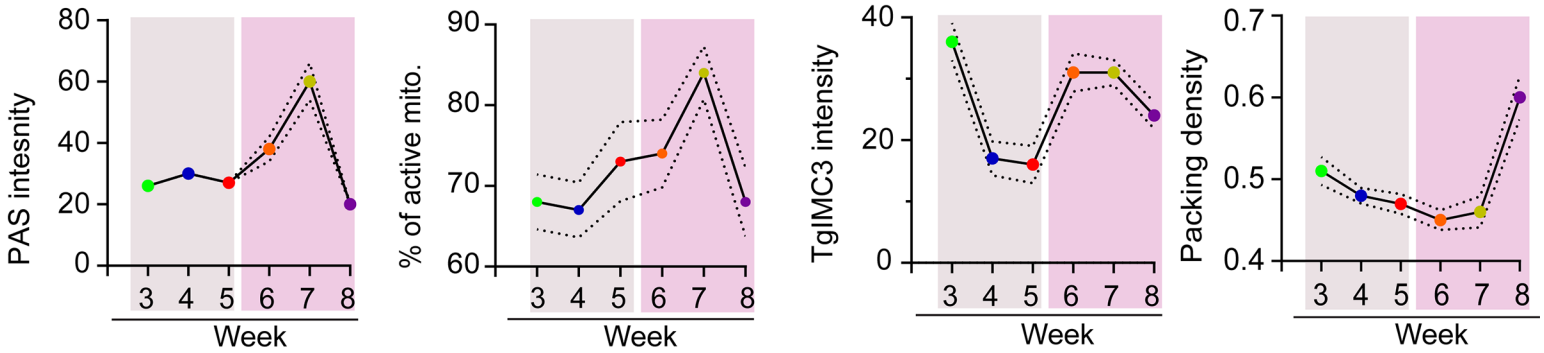

Tripathi et al 2024 **Figure 8**